Method for defect stability diagram from ab initio calculations: A case study of SrTiO_{3}

Amit Samanta, Weinan E, and S. B. Zhang

Phys. Rev. B **86**, 195107 — Published 5 November 2012

DOI: 10.1103/PhysRevB.86.195107

A method for defect stability diagram from ab initio calculations: a case study of SrTiO$_3$

Amit Samanta*
Program in Applied and Computational Mathematics, Princeton University, Princeton, New Jersey 08544, USA

Weinan E
Department of Mathematics and Program in Applied and Computational Mathematics,
Princeton University, Princeton, New Jersey 08544, USA

S. B. Zhang
Department of Physics, Rensselaer Polytechnic Institute, New York 12180, USA

(Dated: September 20, 2012)

Point defects play a dominant role in determining the wide spectrum of electronic and physical properties of semiconducting materials that have vast technological applications. Using ab-initio simulations, a method to calculate equilibrium defect concentrations, Fermi energy and defect stability diagrams as functions of external parameters, such as temperature and pressure, is presented. Using SrTiO$_3$ as a representative material, we report our analysis of the stability of oxygen vacancies and interstitials, in their different charge states, as a function of temperature, oxygen partial pressure and Fermi energy of the system. Further, by analyzing the defect chemistry at experimentally relevant temperatures, we find that at low oxygen partial pressure, neutral oxygen vacancies are most dominant and at intermediate and high oxygen partial pressure, doubly charged oxygen vacancies defects are dominant.

PACS numbers: 82.65.+r

I. INTRODUCTION

An important feature of ionic and electronically conducting materials is the way in which their defect concentrations are related to external factors such as temperature, pressure, doping conditions, etc. For example, materials like Si, ZnO, etc. can switch from n-type conductor to p-type conductor with changes in oxygen partial pressure and doping conditions.[1,2] Similarly, ambient conditions that determine the stability of point defects can affect the stability of phases in systems like ZrO$_2$.[3,4] To understand the effect of external conditions on defect physics of a material, consider the case of an oxide material. The oxygen partial pressure and temperature in the surroundings plays an important role in determining the stability of an oxygen ion in the lattice. For example, the following equilibrium determines the concentration of doubly charged vacancies (V_o^{2+}) in the lattice:

$$\mathrm{O_o} \Longleftrightarrow \frac{1}{2}\mathrm{O_2\,(gas)} + \mathrm{V_o^{2+}} + 2\mathrm{e}^- \tag{1}$$

Physically, this means that the oxygen goes to the atmosphere after being removed from the oxide lattice leaving behind a system containing a vacant oxygen lattice site and two extra electrons. Depending on the equilibrium chemical potential (Fermi energy, μ_e) of the system, the vacant lattice site can trap all or some of these electrons to form a neutral or a charged vacancy.

Ab-initio simulations provide vital information about the structural stability and mobility of point defects in a lattice. However, using ab-initio results for a single defect one can not fully determine the equilibrium defect concentrations for such defect species as the μ_e is not known. This is because, most ab-initio calculations are performed by using a representative simulation cell containing small number of defects. In contrast, a real system in nature contains a variety of defect species in their different charge states. In such samples, μ_e is self-consistently determined by the system depending on the conditions imposed on it by the surroundings. To do this from theoretical calculations, it is imperative to enlist the possible laws of mass action, determine the corresponding rate constants and then using the charge neutrality condition to obtain a self consistent solution of μ_e as a function of the external conditions.

The existence of an unique μ_e is guaranteed if the number of independent laws of mass action equals the number of variables (μ_e, defect concentrations, etc.). Since, each defect in a system has a unique formation energy (depending on the external conditions), it is possible to write down the necessary set of independent reaction equilibria for an ensemble of defect species. Subsequently, once μ_e is obtained by solving the set of nonlinear laws of mass action, the equilibrium defect concentrations can also be determined as a function of the existing external conditions. Using this information, a defect stability diagram, that shows the thermodynamically stable defects under different conditions of temperature (T) and pressure (P), can be plotted. Such diagrams can provide vital information about phase transitions, ionic conductivity, etc. and also help in selecting experimental parameters.[5–7] For example, there is extensive interest in studying transport properties along SrTiO$_3$/LaAlO$_3$ interface.[8–13] Since, experiments suggest a considerable change in the stoichiometry along the interface, an analysis of the thermodynamic stability of the point defects is imperative to understand the transport properties.[3]

Given the importance of the knowledge of equilibrium defect concentrations, there exists extensive literature on defect stability diagrams obtained from large sets of experimental data.[5,6,14–18] Pioneering work in this direction was performed by Brouwer who proposed different scaling laws for oxygen defect (vacancy, interstitial) concentrations in terms of oxygen partial pressure.[5] These scaling laws were then matched with the experimental values of diffusivity and correspondingly the formation and migration energies of point defects were obtained. [14–16,19] Since, performing laboratory experiments under extreme conditions of temperature and pressure can be very expensive, it is desirable to obtain defect stability diagrams from DFT calculations.[20–23]

Here, we use a commonly used perovskite, $SrTiO_3$, as a representative material to study the stability of anionic defects. The crystal structure consists of a simple cubic framework of Sr atoms with Ti atoms occupying the body center position and O occupies the face centers. Thus there are six O surrounding each Ti forming a TiO_6 octahedron with Sr atoms in the cavities of these octahedral. $SrTiO_3$ is an important oxide material that finds use in the semi-conductor industry and also as a fast ion conductor. With an indirect band-gap of 3.25 eV, it belongs to the class of wide-band gap semiconductor and shows optical properties.[24–26] $SrTiO_3$ is oxygen deficient (often exists as $SrTiO_{3-x}$, $0 \leq x \leq 0.5$), which makes it suitable for oxygen sensors and solid state fuel cells.[27] Given the wide spectrum of properties and technological applications, a thorough understanding of the stability and mobility of oxygen vacancies in $SrTiO_3$ is imperative.

The paper is organized as follows: in section II, we describe our calculation methodology and in section III, we present our ab-initio results for the electronic structure, migration barriers and formation energies of anionic defects as functions of Fermi energy of the system, temperature and oxygen partial pressure. In sections IV and V, we provide elaborate description of the possible laws of mass action and a method to obtain equilibrium defect concentrations.

II. METHOD OF CALCULATION

Our results are based on ab-initio calculations performed using the plane wave basis density functional theory code - Vienna Ab-initio Simulation Package (VASP) using PBE (GGA) exchange correlation functional.[28–30] We have used a kinetic energy cutoff of 520 eV and static relaxations have been performed till the forces on individual atoms are smaller than 10^{-4} eV/Å. Further, the pseudo-potentials (PAW type) used have the following valence electronic configurations : Sr : $4s^2 4p^6 5s^2$ (core cutoff radius - 1.323 Å), Ti : $3s^2 3p^6 3d^2 4s^2$ (core cutoff radius - 1.217 Å), O : $2s^2 2p^4$ (core cutoff radius - 0.979 Å).

Using a $1 \times 1 \times 1$ simulation cell of 5 atoms (one Sr, one Ti and three O) and 120 irreducible k-points in the first Brillouin zone we obtain the lattice parameter as 3.945 Å, which is a higher than the experimental value of 3.905 Å.[31–34] For subsequent simulations of defects in $SrTiO_3$ the volume as well as the shape of the cell are frozen. Defect calculations are performed using $2 \times 2 \times 2$ (40 atoms) and $3 \times 3 \times 3$ (135 atoms) simulation cells with 4 and 1 irreducible k-points, respectively, in the first Brillouin zone.

A band gap of 1.82 eV (experimental band-gap is 3.25 eV) is calculated from the difference $E_g = E(N+1) + E(N-1) - 2E(N)$, where $E(N)$ is the energy of the perfect simulation cell containing N electrons.[24–26] Using HSE hybrid functional we obtain a band gap from the difference of the highest occupied and lowest unoccupied eigenlevels of E_g = 3.37 eV when the screening parameter $\mu = 0.30$ Å^{-1}, E_g = 4.11 eV for $\mu = 0.20$ Å^{-1} and E_g = 4.83 eV for $\mu = 0.10$ Å^{-1}. Thus for all subsequent hybrid functional calculations we have used $\mu = 0.30$ and a $2 \times 2 \times 2$ simulation cell (40 atoms). The net force on the system is sensitive to the net charge on the system - for neutral defects the net force is ∼0.03 eV/Å but increases to ∼0.08 eV/Å for charged defects. Diffusion paths and migration barriers are calculated using the Nudged Elastic Band (NEB) method.[35]

Since experiments on $SrTiO_3$ are performed at wide range of temperature and oxygen partial pressures, our defect concentrations are calculated as a function of temperature (100 K to 2000 K) and pressure (10^{-20} atm to 10^{15} atm).[8,36–39] The formation energies are analyzed at representative temperatures of 0 K, 800 K and 1200 K.

A. Reference state calculations

From first-principles calculations of an oxygen molecule using the hybrid functional HSE, we find that the triplet state ($^3\Sigma_g^-$) is ground state of O_2. We find $E_{O_2}^{\mathrm{vasp}}$ = -16.99 eV and a bond length of 1.23 Å. The singlet state is 1.18 eV (PBE result is 1.03 eV) higher than the triplet state. The energy of an oxygen obtained from spin polarized calculations is $E_{\mathrm{O}}^{\mathrm{vasp}}$ = -5.83 eV, yielding a dissociation energy of 5.33 eV which is little higher than the experimental value of 5.12 eV.[40] The dissociation energy obtained from PBE (GGA) exchange correlation functional (using 10 irreducible k-points) is 6.64 eV.

The dependence of the chemical potential (μ_{O_2}) of an oxygen gas molecule on temperature and oxygen partial pressure can be estimated from the quantum formulation of an ideal gas. Taking into consideration the translational, vibrational and rotational contributions, the chemical potential of an oxygen molecule is given by :[41]

$$\mu_{O_2} = k_{\mathrm{B}}T \log\left(\frac{P\lambda^3}{k_{\mathrm{B}}T}\right) - k_{\mathrm{B}}T \log\left(\frac{Ik_{\mathrm{B}}T}{\hbar^2}\right) + \frac{1}{2}\hbar\omega_{\mathrm{o}} + k_{\mathrm{B}}T \log\left[1 - \exp\left(-\frac{\hbar\omega_{\mathrm{o}}}{k_{\mathrm{B}}T}\right)\right] \tag{2}$$

where, λ is the thermal de Broglie wavelength, k_{B} is the Boltzmann constant, $\hbar$ is the reduced Planck's constant and I is the moment of inertia of the oxygen molecule. From ab-initio calculations, we find the vibrational frequency of O_2 is ω_{o} = 1568.06 cm^{-1}, which is close to experimental result of ω_{o} =1565.4 cm^{-1}.[42] For our subsequent analysis, the chemical potential of an oxygen atom is taken as half of μ_{O_2} :

$$\mu_{\mathrm{O}}\left(T,P\right)=\frac{1}{2}\mu_{\mathrm{O}_2}\left(T,P\right) \tag{3}$$

Fig. 1 shows the variation in the oxygen chemical potential with temperature at different oxygen partial pressures.

III. FORMATION ENERGY OF ANIONIC DEFECTS

A. Oxygen Vacancy

Oxygen ions in $SrTiO_3$ form a tetragonal lattice with parameters $a_{\mathrm{o}}/\sqrt{2}$, $a_{\mathrm{o}}/\sqrt{2}$ and a_{o}, where a_{o} is the lattice parameter of the defect free $SrTiO_3$ unit cell. The formation of oxygen vacancies in $SrTiO_3$ have been studied previously using theoretical as well as experimental techniques.[43–46] In laboratory experiments, oxygen vacancies can be introduced in a $SrTiO_3$ sample by varying the external oxygen partial pressure and temperature or via various processes such as growth, annealing, and redox reactions. In our simulation setup, an oxygen vacancy formed by removing an oxygen atom from the defect free neutral cell results in an inward movement of the nearest neighbor (NN) anions and cations. The NN oxygens move towards the vacant site by 0.21 Å (7.42 $\%$ of the original bond length) along $\langle 110\rangle$ direction. The next nearest neighbor oxygen ions move away from the vacant site by 0.17 Å (4.19 $\%$ of the original separation) along the $\langle 100\rangle$ direction. In contrast, the nearest neighbor cations (both Sr and Ti ions) move away from the vacant oxygen lattice site. The four NN Sr coplanar with the oxygen vacancy in the neutral cell move out by 0.11 Å along $\langle 110\rangle$ directions while the Ti ion moves outwards by 0.12 Å along $\langle 100\rangle$ direction. The four Sr ions and the two Ti ions together form a octahedron with the oxygen vacancy lying at the center of the octahedron. Volume relaxations are performed by allowing the lattice vectors and the shape of the simulation cell to change. We find volume relaxation breaks the cubic symmetry of the original supercell and the relaxed cell has tetragonal symmetry. The decrease in volume is 1.45 Å^3 for the 40 atoms supercell and 1.88 Å^3 for the 135 atoms supercell, while the decrease in energy is negligibly small (only 4 meV in a 135 atoms supercell).

Using a 40 atoms simulation cell we find the system has a non-zero magnetization and the triplet state has 0.21 eV lower energy than the singlet state.[47] However, using a 135 atoms and 320 atoms simulation cell we find that the singlet state (zero residual spin) is the ground state.[48] Fig. 2 shows the spin density profile for an oxygen vacancy in a 40 atoms supercell under neutral charge conditions. This shows the extensive hybridization between the $3d$-e$_g$ orbitals of the NN Ti and the two electrons localized at the vacant anionic site.[49,50]

A singly and doubly charged oxygen vacancy is formed by removing one and two electrons, respectively, along with an oxygen atom from the defect free system. The local lattice near the vacancy in case of charged computation cells show greater distortions than a neutral cell. The spin density for a singly charged vacancy has a profile similar to a vacancy in a neutral cell (Fig. 2). Similar to the case of a vacancy in a neutral cell, using a $2{\times}2\times 2$ supercell we find the triplet state has 0.03 eV lower energy than the singlet state.[47] However, the stability is reversed when a larger (135 atoms) simulation cell is used, i.e. an isolated V_{o}^{+} has zero magnetization in ground state. A doubly charged vacancy in a $2{\times}2\times 2$ and $3{\times}3\times 3$ simulation cell has zero magnetization.

For a singly charged oxygen vacancy, volume relaxation results in decrease in volume of the cell by 7.66 Å^3 ($2{\times}2\times 2$ simulation cell) and a 0.07 eV decrease in energy. Similarly, for a doubly charged vacancy, the decrease in volume is 15.47 Å^3 and the energy decreases by 0.26 eV. The relaxation volume for the charged vacancies must take into account the presence of electrons in the system. In a defect free $SrTiO_3$ supercell, the addition of an extra electron and subsequent volume relaxation results in decrease in energy of the system by 0.05 eV and the volume increases by 9.42 Å^3. So the relaxation volume for singly charged oxygen vacancy is 1.76 Å^3 and for a doubly charged oxygen vacancy is 3.37 Å^3.

There is a large spread in values of oxygen diffusion barriers reported for $SrTiO_3$.[43,44,46] Recent anelastic relaxation measurements on $SrTiO_3$ crystal report a barrier of 0.60 eV for hopping of isolated vacancies.[44] For an oxygen vacancy in a neutral cell we find diffusion along $\langle 110\rangle$ direction has the lowest energy barrier. In this case, an oxygen vacancy moves from one face-centered site to another in the same TiO_6 octahedral structure. Since the oxygen sub-lattice is tetragonal in nature, there are two possible paths for ion migration along the two different lattice vectors of the oxygen sub-lattice. One path is along $\langle 100\rangle$ direction (Fig. 3) and the other is along $\langle 110\rangle$ direction (Fig. 4). The $\langle 100\rangle$ path involves movement of the vacancy from one face centered site to another site in different TiO_6 octahedron. The saddle point configuration in this case is similar to the $\langle 100\rangle$ crowd-ion configuration. Since the crowd-ion site is a high energy site, the barrier is considerably higher than the barrier along $\langle 110\rangle$ direction. Table I shows the barriers for diffusion of oxygen vacancy in a neutral and charged supercell. The diffusion barrier along $\langle 110\rangle$ direction decreases with increase in charge on simulation cell.

Defect	$\langle 100\rangle$	$\langle 110\rangle$
V_o	3.09	0.63
V_o^{1+}	3.02	0.54
V_o^{2+}	2.66	0.39
O_i	1.96	-
O_i^{1-}	1.36	-
O_i^{2-}	1.25	-

TABLE I: Migration barrier for different charge states of anionic defects in $SrTiO_3$ calculated using PBE functional in a 135 atoms simulation cell.

Physically, in a material exposed to atmosphere, the process of vacancy formation (say V_o^{2+}) can be described by the equilibrium in (1). The corresponding vacancy formation energy is given by

$$E_f\left(\mathrm{V}_o^{n+}\right) = E\left(\mathrm{SrTiO_3} + \mathrm{V}_o^{n+}\right) - E\left(\mathrm{SrTiO_3}\right) + \mu_{\mathrm{O}} + n\mu_e \tag{4}$$

where, $E\left(\mathrm{SrTiO_3} + \mathrm{V}_o^{n+}\right)$ is the energy of a simulation cell containing a vacant oxygen lattice site and a net positive charge of $+ne$, $E\left(\mathrm{SrTiO_3}\right)$ is the energy of a defect free $SrTiO_3$ cell and μ_e is the chemical potential of the electrons. Fig. 5 shows the formation energy of an oxygen vacancy as a function of Fermi level at T = 0 K and T = 800 K at different oxygen partial pressures for PBE and HSE functionals. The formation of a neutral oxygen vacancy from PBE functional is about 5 eV while using the HSE functional we obtain a value of 4 eV at 0 K. At 800 K and 1 atm pressure, PBE results suggest 4.13 eV while HSE results yields 3.11 eV. At both these temperatures, when the Fermi level is near the valence band edge, V_o^{2+} is the most stable charge state of a vacancy, but at higher Fermi levels neutral charge state (V_o) becomes energetically favorable. However, depending on P and T, below a critical μ_e the system becomes unstable and V_o^{2+} can form spontaneously, for example, at 800 K and 10^{-8} atm, for μ_e below 1.50 eV, the system becomes unstable. With decrease in oxygen partial pressure the formation energy of a vacancy also goes down. For example, at 800 K the formation energy of a neutral vacancy decreases from 3.14 eV at 1 atm to 2.82 eV at 10^{-4} atm and further down to 2.51 eV at 10^{-8} atm. Some probable defect reactions involving oxygen vacancies are tabulated in Table III. Since, the reaction $V_o^{2+} + V_o^0 \Rightarrow 2V_o^{1+}$ increases the energy by 0.23 eV, our results suggest that singly charged oxygen vacancies are unstable in $SrTiO_3$.

B. Oxygen Interstitial

We find that oxygen interstitials in $SrTiO_3$ can have different possible atomic structures: (i) $\langle 110\rangle$ dumbbell, Fig. $6(a)$, (ii) $\langle 100\rangle$ crowd-ion, Fig. $6(b)$ and (iii) $\langle 100\rangle$ dumbbell, Fig. $7(a)$. For ease of reference the interstitial configurations are labeled as $O_{\langle 110\rangle}$, $O_{\langle 100\rangle}$ for the $\langle 110\rangle$ and $\langle 100\rangle$ dumbbell configurations, respectively, and $O_{\langle 100c\rangle}$ for $\langle 100\rangle$ crowd-ion configuration. The $\langle 110\rangle$ dumbbell and $\langle 100\rangle$ dumbbell have dumbbell centers on the original oxygen lattice site. The relative stability of different interstitial configurations with respect to $O_{\langle 100\rangle}$ are shown in Table II. For an oxygen interstitial with neutral charge, the $O_{\langle 100\rangle}$ configuration is energetically most favorable. The dumbbell separation is 1.62 Å, little higher that the O-O bond length in peroxides.[51,52] Incorporation of an extra oxygen atom in a neutral cell results in outward movement of the nearest neighbor cations. For example, the Sr atoms on the $\{100\}$ plane containing the dumbbell move outward by 0.27 Å along $\langle 1\bar{1}0\rangle$ direction. Similarly, the Ti-Sr NN distance increases by 0.13 Å. For $O_{\langle 100\rangle}$ structure, we find the relaxation volume is 7.69 $Å^3$, which is about a third of the oxygen atomic volume (14 cm^3mol^{-1}). Volume relaxation destroys the cubic symmetry of the simulation cell and the resulting structure has orthorhombic symmetry.

The valence charge localized on the dumbbell is analyzed from the total charge density of the system using charge integration over a Voronoi cell enclosing these ions.[53,54] In a neutral cell, the charge on both the oxygen ions is in the range of -0.78e to -0.89e, where e is the unit electronic charge.[55] This charge sharing shows the extent of hybridization taking place between the $2p$-orbitals of the oxygens in the dumbbell. The site projected density of states (PDOS), Fig. $8(a)$, for an oxygen ion in the $\langle 100\rangle$ dumbbell is similar to that of an oxygen gas molecule (O_2) with two localized electrons. The ground state structure of O_2 is the triplet state ($^3\Sigma_g^-$) and has one electron in each of the π_{2p}^* anti-bonding molecular orbitals resulting in two unpaired electrons. Adding two electrons to the system fills up the originally half filled π_{2p}^* molecular orbitals and the resulting structure has no net magnetization. A similar scheme of overlap seems to exist for the $O_{\langle 110\rangle}$ geometry.

For an oxygen interstitial in a 135 atoms supercell we find that the local electronic density of states near one of the dumbbell ions are the same for spin up and spin down in $O_{\langle 110\rangle}$ and $O_{\langle 100\rangle}$ and hence there is no residual spin in the system. In contrast, oxygen interstitials in $O_{\langle 100c\rangle}$ do have residual spin for the smaller as well as the larger supercells. Fig. $8(b)$ shows the site

Defect	Interstitial	$O_{\langle 100\rangle}$	$O_{\langle 110\rangle}$	$O_{\langle 100c\rangle}$
O_i^0	Energy (relative, eV)	0	0.68	1.96
	Dumbbell separation (Å)	1.62	1.64	-
O_i^{1-}	Energy (relative, eV)	0	0.75	1.36
	Dumbbell separation (Å)	2.18	2.15	-
O_i^{2-}	Energy (relative, eV)	0	0.81	1.25
	Dumbbell separation (Å)	2.42	2.46	-

TABLE II: Relative stability and dumbbell separations for neutral and charged oxygen interstitials in $SrTiO_3$ for a 135 atoms simulation cell obtain from PBE calculations. The defect energy values have not been corrected for periodic interactions. For neutral and charged oxygen interstitials the $\langle 100\rangle$ is the ground state configuration.

projected DOS of the oxygen interstitial in the crowd-ion configuration (40 atoms cell).

The lowest barrier path for interstitial diffusion in a neutral cell is along $\langle 100\rangle$ direction. Fig. 7 shows the intermediate configurations during the diffusion process (the oxygens in the dumbbell are marked O1, O2). In the first step, O2 detaches from O1 and moves closer to the $\langle 100\rangle$ crowd-ion site (saddle configuration). The total length of the diffusion path is 5.38 Å while the distance between the initial and final configuration is 2.72 Å and the migration barrier is 1.96 eV.

Next, we consider a system with an interstitial and an extra electron. The lowest energy configuration in this case is the $\langle 100\rangle$ dumbbell. Using a 135 atoms cell we find that the system has zero magnetization whereas a 40 atoms supercell containing an interstitial and extra electron in its relaxed state has a non-zero magnetization. The increase in electro-static repulsion between the ions and the extra electron in the cell, results in a greater dumbbell separation of 2.18 Å. The presence of an extra electron results in inward movement of the cations compared to a defect free simulation cell. For example, the Ti-Sr bond length shows only a marginal increase of 0.04 Å compared to a pure cell. Similarly, the each Sr on a $\{100\}$ plane containing the dumbbell moves outward only by 0.16 Å. The anions, on the other hand, show small a ($\sim$0.05 Å) outward movement.

Volume relaxations are performed by allowing the shape and the lattice parameters to change. For the singly charged cell with an interstitial the volume increases by 17.25 $Å^3$ and the decrease in energy is 0.31 eV. However, the total relaxation volume must also incorporate the change in volume of the cell due to the free electron. For a 40 atoms cell, we find the volume of the cell decreases by 7.14 $Å^3$ and the energy decreases by 0.05 eV due to the removal of an electron. Thus the relaxation volume of a singly charged oxygen interstitial is 10.11 $Å^3$.

Diffusion of oxygen interstitial in singly charged cell is similar to that in the neutral cell. However, in this case there is an increase in the net charge on the diffusing oxygen ion which leads to greater distortion of the local lattice and increased nearest neighbor separations. This results in a lower migration barrier of 1.36 eV. The separation between the initial and the final locally stable configurations in the multidimensional configuration space is 2.71 Å. The saddle configuration is an oxygen interstitial in crowd-ion configuration.

For doubly charged oxygen interstitials (dumbbell separation is 2.42 Å) there is greater distortion of the lattice as the presence of two extra electrons increases the electro-static interaction with the host ions. Similar is the case of the interstitial in the $\langle 110\rangle$ dumbbell configuration. The lowest energy diffusion path is along $\langle 100\rangle$ direction. The saddle configuration is crowd-ion configuration and the energy barrier is 1.25 eV. The charge density difference between doubly and singly charged oxygen interstitials shows the σ^* character of the defect state. Volume relaxation of the ground state structure results in an increase in the volume of the cell by 27.38 $Å^3$. As in the neutral and singly charged cell, the volume relaxation results in a orthorhombic cell. Taking into account the relaxation effects of the two holes, we obtain a relaxation volume of 13.11 $Å^3$ for an interstitial in a doubly charged cell.

In a laboratory experiment, the process of formation of O_i^{2-}, can be understood by the following reaction :

$$\frac{1}{2}\mathrm{O_2\,(gas)} \Longleftrightarrow \mathrm{O_i^{2-}} + 2\mathrm{h}^{1+}. \tag{5}$$

Fig. 5 shows the formation energy of O_i^{2-}, O_i^{1-} and O_i^0 as a function of the Fermi energy of the system at T = 0 K and T = 800 K. With increasing temperature incorporation of oxygen interstitials become energetically expensive. For example, the incorporation of neutral interstitial at T = 0 K costs about 2.18 eV (HSE) but at T = 800 K and 1 atm pressure the formation energy is = 2.99 eV (HSE). In contrast, according to PBE functional neutral interstitial costs 1.81 eV at 0 K and 2.76 eV at 800 K, 1 atm. From these plots, we also find that O_i^{1-} is energetically not favorable at any Fermi level in $SrTiO_3$.

Table III shows some of the possible reactions between the anionic defects in $SrTiO_3$ and their reaction energies. These reaction energies are calculated at 0 K and zero pressure assuming dilute concentration of the defect species. A positive energy means the forward reaction is unfavorable. For example, the formation of singly charged interstitials from a pair of doubly charged and neutral interstitial costs 0.10 eV (HSE). DFT (PBE) results for reactions 6-8 suggest that a pair of neutral vacancy

No.	Reaction	Energy (eV, PBE)	Energy (eV, HSE)
1	O_i^{2-}+O_i^0⇒2O_i^{1-}	-0.14	0.10
2	V_o^{2+}+V_o^0⇒2V_o^{1+}	-0.11	0.23
3	Null ⇒O_i^0+V_o^0	$\Delta H_F^{''}$= 6.80	6.14
4	Null ⇒O_i^{1-}+V_o^{1+}	$\Delta H_F^{'}$= 6.74	6.68
5	Null ⇒O_i^{2-}+V_o^{2+}	ΔH_F= 5.69	6.90
6	O_i^0+V_o^0⇒O_i^{1-}+V_o^{1+}	-0.06	0.55
7	O_i^{1-}+V_o^{1+} ⇒O_i^{2-}+V_o^{2+}	0.31	0.21
8	O_i^0+V_o^0 ⇒O_i^{2-}+V_o^{2+}	0.37	0.76
9	Null ⇒e^-+h^+	E_g= 3.25	3.37

TABLE III: Defect reactions and the corresponding energy change at T = 0 K. The energy change is obtained from the formation energy of the defects. The PBE results correspond to a 135 atoms simulation cell while the HSE results correspond to 40 atoms cell.

and neutral interstitial would prefer to form at the cost of a pair of singly charged or doubly charged Frenkel defect. This is in contrast to results from HSE hybrid functional calculations.

IV. DEFECT EQUILIBRIUM REACTIONS

The thermodynamic stability of different point defects can be understood by writing down the equilibrium chemical reactions (laws of mass action).[6] Apart from the laws of mass action, the various point defects present must also satisfy the electronic charge neutrality condition. We consider the stable anionic defects in $SrTiO_3$, namely O_i, O_i^{2-}, V_o and V_o^{2+} in their lowest energy configuration. Possible reactions involving O_i^{2-} and V_o^{2+} are:

$$\mathrm{O}_o \Longleftrightarrow \mathrm{O}_i^{2-} + \mathrm{V}_o^{2+} \qquad K_F = \frac{\left[\mathrm{O}_i^{2-}\right]\left[\mathrm{V}_o^{2+}\right]}{N_a^2} \tag{6}$$

$$\mathrm{O}_o \Longleftrightarrow \frac{1}{2}\mathrm{O}_2\,(gas) + \mathrm{V}_o^{2+} + 2\mathrm{e}^- \qquad K_1 = \frac{\left[\mathrm{V}_o^{2+}\right]\left[\mathrm{e}^-\right]^2}{N_a N_c^2} P^{1/2} \tag{7}$$

$$\mathrm{Null} \Longleftrightarrow \mathrm{e}^- + \mathrm{h}^+ \qquad K_i = \frac{\left[\mathrm{h}^+\right]\left[\mathrm{e}^-\right]}{N_v N_c} = e^{-E_g/k_B T} \tag{8}$$

$$\frac{1}{2}\mathrm{O}_2\,(gas) \Longleftrightarrow \mathrm{O}_i^{2-} + 2\mathrm{h}^+ \qquad K_2 = \frac{\left[\mathrm{h}^+\right]^2\left[\mathrm{O}_i^{2-}\right]}{N_v^2 N_a P^{1/2}} \tag{9}$$

which describe the formation of Frenkel defects in the anionic sub-lattice, the formation of an oxygen vacancy by losing oxygen to the atmosphere, the formation of electron-hole pair and the formation of oxygen interstitial, respectively. Here, $\left[\mathrm{e}^-\right]$ and $\left[\mathrm{h}^+\right]$ are the electron and hole concentration, respectively, $\left[\mathrm{O}_i^{2-}\right]$ is the oxygen interstitial concentration, $\left[\mathrm{V}_o^{2+}\right]$ is the oxygen vacancy concentration, N_a is the concentration of anionic sites and E_g is the band gap. $N_c = 2\left(2\pi m_e^* k_B T/h^2\right)^{3/2}$ and $N_v = 2\left(2\pi m_h^* k_B T/h^2\right)^{3/2}$ are the constants used to normalize the electron and hole concentrations.[6] Further, considering only the doubly charged anionic defects, the charge neutrality condition is:

$$2\left[\mathrm{O}_i^{2-}\right] + \left[\mathrm{e}^-\right] = 2\left[\mathrm{V}_o^{2+}\right] + \left[\mathrm{h}^+\right] \tag{10}$$

Since $K_F = e^{-\Delta H_F/k_B T}$ and $K_i = e^{-E_g/k_B T}$, using values from Table III, we find $K_F \ll K_i$. Hence the concentrations of $[h^+]$, $[e^-]$ are much higher than the doubly charged Frankel defects. In this limit, at intermediate oxygen partial pressure, the charge neutrality equation can be simplified (Brouwer approximation)[5] to $[e^-]$ = $[h^+] \propto \sqrt{K_i}$.

When the oxygen partial pressure is increased, eq (9) shifts right and we get more oxygen interstitials. Similarly, when the pressure is decreased, eq (7) shifts right yielding more oxygen vacancies. Thus using the above approximation for electron and hole concentration, we obtain a scaling relationship between the concentration of oxygen interstitials and vacancies and the oxygen partial pressure P:

$$\left[{V_o}^{2+}\right] \propto P^{-1/2} \qquad \left[{O_i}^{2-}\right] \propto P^{1/2}. \tag{11}$$

At very low oxygen pressure, the charge neutrality condition reduces to $[e^-] = 2\left[V_o^{2+}\right]$ which means, $\left[\mathrm{V}_o^{2+}\right] \propto P^{-1/6}$. Similarly, at high oxygen partial pressures $\left[{\mathrm{O}_i}^{2-}\right] \propto P^{1/6}$.

For the neutral defects the thermodynamic equilibrium reactions for O_i and V_o are given by:

$$\begin{aligned}
\mathrm{O}_o &\Longleftrightarrow \mathrm{O}_i + \mathrm{V}_o & K_F^{''} &= \frac{[\mathrm{O}_i]\,[\mathrm{V}_o]}{N_a^2} \\
\mathrm{O}_o &\Longleftrightarrow \frac{1}{2}\mathrm{O}_2\,(gas) + \mathrm{V}_o & K_1^{''} &= \frac{[\mathrm{V}_o]\,P^{1/2}}{N_a} \\
\frac{1}{2}\mathrm{O}_2\,(gas) &\Longleftrightarrow \mathrm{O}_i & K_2^{''} &= \frac{[\mathrm{O}_i]}{N_a P^{1/2}}
\end{aligned} \tag{12}$$

which describe the formation of Frankel defects in the anionic sub-lattice, the formation of an oxygen vacancy by loosing oxygen to the atmosphere and the formation of oxygen interstitial. Solving the above we get

$$[\mathrm{O}_i] \propto P^{1/2} \qquad [\mathrm{V}_o] \propto P^{-1/2} \tag{13}$$

V. DETERMINATION OF EQUILIBRIUM FERMI ENERGY

The formation energy plots provide information about the stability of different point defects as a function of temperature, pressure and Fermi energy of the system. Consider for example, defect formation energies at 800 K and 1 atm as shown in Fig. $5(d)$. For Fermi energy values less than 1.18 eV the system becomes unstable leading to spontaneous formation of doubly charged oxygen vacancies. If the chemical potential lies in between 1.18-2.65 eV, the system will have many charged vacancies due to which the system will not be electronically neutral. So the Fermi energy (μ_{e}) of the system is constrained to lie between 2.65 eV and 3.15 eV. However, a crucial element missing in this analysis is the contribution from electrons and holes. Even though the Frenkel pair formation energies (see Table III) are much higher than the band gap, individual defect formation energies can be comparable to the optical bang gap (Fig. 5). The charge neutrality condition for undoped $\mathrm{SrTiO_3}$ containing only anionic defects is:

$$2\left[\mathrm{O}_i^{2-}\right] + \left[\mathrm{O}_i^{1-}\right] + \left[\mathrm{e}^-\right] = 2\left[\mathrm{V}_o^{2+}\right] + \left[\mathrm{V}_o^{1+}\right] + \left[\mathrm{h}^+\right]. \tag{14}$$

The dominant defect equilibria that can be derived from the charge neutrality condition are tabulated in Table IV.

In Table IV the equilibrium reactions (1)-(7), except (5), correspond case when electron and hole concentrations are equal to the ionic defect concentrations. Hence, these regimes correspond to electronic conductivity. On the other hand, reactions (8)-(12) correspond to the regime where ionic conductivity is dominant. Further, we plot the defect concentrations at 800 K and 1 atm pressure as a function of the Fermi energy as shown in Fig. 10. The defect concentrations are calculated from the rate constants derived from the laws of mass action, namely, (9). For instance, the doubly charged oxygen vacancy concentration is given by

$$\left[\mathrm{V}_o^{2+}\right] = \frac{N_a N_c^2 K_1}{\left[\mathrm{e}^-\right]^2} \qquad K_1 = e^{-\Delta E\left(\mathrm{V}_o^{2+}\right)/k_B T} \tag{15}$$

where, K_1 is the rate constant and

$$\Delta E\left(\mathrm{V}_o^{2+}\right) = E\left(\mathrm{SrTiO_3} + \mathrm{V}_o^{2+}\right) + \mu_O - E\left(\mathrm{SrTiO_3}\right) \tag{16}$$

where, $E\left(\mathrm{SrTiO_3} + \mathrm{V}_o^{2+}\right)$ is the energy of the relaxed simulation cell containing a doubly charged vacancy and $E\left(\mathrm{SrTiO_3}\right)$ is

No.	Reaction
1	$2\left[\mathrm{O}_i^{2-}\right]=\left[\mathrm{h}^{+}\right]$
2	$\left[\mathrm{O}_i^{1-}\right]=\left[\mathrm{h}^{+}\right]$
3	$2\left[\mathrm{V}_o^{2+}\right]=\left[\mathrm{e}^{-}\right]$
4	$\left[\mathrm{V}_o^{1+}\right]=\left[\mathrm{e}^{-}\right]$
5	$\left[\mathrm{e}^{-}\right]=\left[\mathrm{h}^{+}\right]$
6	$2\left[\mathrm{O}_i^{2-}\right]=\left[\mathrm{V}_o^{1+}\right]+\left[\mathrm{h}^{+}\right]$
7	$2\left[\mathrm{V}_o^{2+}\right]=\left[\mathrm{O}_i^{1-}\right]+\left[\mathrm{e}^{-}\right]$
8	$\left[\mathrm{V}_o^{2+}\right]=\left[\mathrm{O}_i^{2-}\right]$
9	$\left[\mathrm{V}_o^{1+}\right]=\left[\mathrm{O}_i^{1-}\right]$
10	$2\left[\mathrm{V}_o^{2+}\right]+\left[\mathrm{V}_o^{1+}\right]=2\left[\mathrm{O}_i^{2-}\right]+\left[\mathrm{O}_i^{1-}\right]$
11	$2\left[\mathrm{O}_i^{2-}\right]=\left[\mathrm{V}_o^{1+}\right]$
12	$2\left[\mathrm{V}_o^{2+}\right]=\left[\mathrm{O}_i^{1-}\right]$

TABLE IV: Probable anionic defect reactions in $\mathrm{SrTiO_3}$ that can maintain charge neutrality balance.

the energy of a pure $\mathrm{SrTiO_3}$ simulation cell. Similarly, the concentration of a doubly charged oxygen interstitial is given by

$$\left[\mathrm{O}_i^{2-}\right]=\frac{N_a N_v^2 K_2}{\left[\mathrm{h}^{+}\right]^2} \qquad K_2=e^{-\Delta E\left(\mathrm{O}_i^{2-}\right)/k_B T} \tag{17}$$

where, K_2 is the rate constant and

$$\Delta E\left(\mathrm{O}_i^{2-}\right)=E\left(\mathrm{SrTiO_3}+\mathrm{O}_i^{2-}\right)-\mu_O-E\left(\mathrm{SrTiO_3}\right). \tag{18}$$

Here, $E\left(\mathrm{SrTiO_3}+\mathrm{O}_i^{2-}\right)$ is the energy of the equilibrium geometry of a doubly charged oxygen interstitial. The electron and hole concentrations are obtained by $\left[\mathrm{e}^{-}\right]=N_c e^{-(E_c-\mu)/k_B T}$ and $\left[\mathrm{h}^{+}\right]=N_v e^{-(\mu-E_c)/k_B T}$.

The different possible equilibrium reactions (Table IV) correspond to the intersection between the formation energies of the defect species. For example, in Fig. $10(a)$ the intersection between the formation energy curves of $\left[\mathrm{V}_i^{2+}\right]$ and $\left[\mathrm{e}^{-}\right]$ corresponds to reaction (3) in Table IV. Similarly, the intersection between the formation energy curves of $\left[\mathrm{V}_i^{2+}\right]$ and $\left[\mathrm{O}_i^{2-}\right]$ determines the equilibrium between the doubly charged species (reaction 8 in Table IV). Since the defect species with highest concentration dominates, consequently at 800 K and $P=1$, 10^{-4}, 10^{-8} atm, the Fermi energy is determined by the equilibrium between $\left[\mathrm{V}_i^{2+}\right]$ and $\left[\mathrm{e}^{-}\right]$. Similarly, at 800 K and $P=1$, 10^{-4}, 10^{-8} atm, the Fermi energy of the system is determined by the coupled system of equations :

$$2\left[\mathrm{O}_i^{2-}\right]+\left[\mathrm{e}^{-}\right]=\left[\mathrm{h}^{+}\right]. \tag{19}$$

Substituting from (17) and reaction (5) in Table IV we get a cubic equation in terms of the hole concentration:

$$\frac{2N_a N_v^2 K_2}{\left[\mathrm{h}^{+}\right]^2}+\frac{N_v N_c K_i}{\left[\mathrm{h}^{+}\right]}=\left[\mathrm{h}^{+}\right]\Rightarrow\left[\mathrm{h}^{+}\right]^3-N_v N_c K_i\left[\mathrm{h}^{+}\right]-2N_a N_v^2 K_2=0 \tag{20}$$

where, K_2 depends on the oxygen partial pressure while both K_i, K_2 are dependent on the temperature. Thus by picking a particular point (P, T) on the parameter space the reaction constants are uniquely determined and so are the concentration of the defect species. With decrease in oxygen partial pressure, the Fermi energy will stay mid-gap (for example at 0.1 atm, see $10(b)$). However, with increase in pressure the equilibrium reaction (1) will dominate. At oxygen partial pressure close to 10^{-8} atm, the Fermi energy is determined by the coupled reaction:

$$2\left[\mathrm{V}_\mathrm{o}^{2+}\right]+\left[\mathrm{h}^{+}\right]=\left[\mathrm{e}^{-}\right] \tag{21}$$

which can be simplified to

$$\frac{2N_a N_c^2 K_1}{\left[\mathrm{e}^{-}\right]^2}+\frac{K_i}{\left[e^{-}\right]}=\left[e^{-}\right]\Rightarrow\left[e^{-}\right]^3-N_v N_c K_i\left[e^{-}\right]-2N_a N_c^2 K_1=0 \tag{22}$$

where, K_1 is dependent on the oxygen partial pressure and the temperature. Thus the analysis of stability of point defects in $\mathrm{SrTiO_3}$ shows existence of different regions stability.

Fig. 11 and Fig. 12 shows the equilibrium concentrations of anionic point defects in $\mathrm{SrTiO_3}$ as a function of oxygen partial pressure at 800 K and 1200 K based on HSE and PBE (without scaling) functional results. At 800 K, the dominant defect species is the doubly charged oxygen vacancy for most physically relevant oxygen partial pressures according to HSE results. The charge neutrality condition in the system is maintained by the equilibrium between V_o^{2+} and free electrons in the system. However, from the PBE results, we see a cross over in the dominant defect species from double charged oxygen interstitials to doubly charged oxygen vacancies with decrease in P. At 1200 K (HSE calculations), for $P > 10^{-12}$ atm, the charge neutrality condition is maintained by equilibrium between electrons and doubly charged oxygen vacancies. However, with decrease in oxygen partial pressure, neutral oxygen vacancies become dominant and the charge neutrality condition is maintained the equilibrium between singly charged oxygen vacancies and the electrons. On the other hand, the PBE calculations suggest that the dominant defect species changes from O_i^{2+} to V_o^{2+} and finally V_o with decrease in oxygen partial pressures. The defect concentration profiles obtained from PBE results followed by scaling the defect transition levels have a similar nature as HSE results.

Based on these defect concentrations, a thermodynamic stability plot can easily be generated. Fig. 13 - 14 shows the stability plot for anionic defects in $\mathrm{SrTiO_3}$ generated by solving the different defect equilibria and assuming that the atmosphere is the source as well as the sink for oxygen. Fig. $13(a)$ shows the stability of defects obtained from PBE calculations. At high temperature and low pressure neutral oxygen vacancies are stable, while, at low temperature and high oxygen pressure oxygen interstitials are stable. At intermediate temperature and pressure conditions, doubly charged oxygen vacancies are most stable. The dominant laws of mass action that preserves the electronic charge neutrality are marked in the figure. When the defect levels are scaled according to the ratio of experimental to calculated band gap, the defect stability diagram is different (Fig. $13(b)$). In contrast to Fig. $13(a)$, we find that oxygen interstitials are not dominant under physically relevant temperature and pressure conditions. The stability diagram obtained from HSE is shown in Fig. 14. The results of HSE functional and PBE functional (with scaling of energy levels) suggest a similar trend.

A generic problem of analyzing the thermodynamic stability of defects using the procedure described here is that the defect species are assumed to be isolated and in dilute concentrations. This assumption is violated at low oxygen partial pressures and high temperatures, for example at 1200 K and pressure less than 10^{-15} atm (see Fig. $12(b)$) anionic defects occupy as much as 10^{-3} fraction of anionic sites. With increase in defect concentrations, there is a significant increase in the Coulomb interaction between these defects which results in local lattice distortions. This can change the stability of isolated defects resulting in the formation of defect clusters. Ideally, one can repeat the procedure described here for defect clusters of different sizes and obtain an elaborate description of their stability but we have neglected them for the current analysis.

VI. CONCLUSIONS

An ab-initio study of ground state structure of anionic point defects in $\mathrm{SrTiO_3}$ are reported. For a neutral and charged oxygen interstitial the energetically favorable configuration is the $\langle 100\rangle$ dumbbell. The different geometries for oxygen interstitials and hybridization scheme between the oxygen ions in the dumbbell in $\mathrm{SrTiO_3}$ is similar to those reported for oxides like MgO (rock salt structure) and cubic $\mathrm{ZrO_2}$ ($\mathrm{CaF_2}$ structure) even though their crystal structures are different.[4,56] We find the relaxation volume of oxygen interstitials (7.69-13.11 Å^3) are dependent on their charge. The high relaxation volumes signify that creep deformation can play a significant role in this material as suggested by recent experiments.[57,58] This is because the stability of vacancies in a stressed solid is related to the work done ($\sigma_{ij}\Omega_{ij}$) by an external stress field (σ_{ij}), where Ω_{ij} is the relation volume tensor and σ_{ij} is the applied stress.

Electronic structure of oxygen vacancies also show interesting properties. In the neutral and singly charged cell, there is significant overlap between the $3d$-orbitals (d_{z^2}) of the two neighboring Ti ions and the holes in the vacant lattice site. The z-axis in this case is oriented along the line connecting the two Ti and ions and the vacancy oxygen lattice site ($\langle 100\rangle$ direction). The magnetic behavior of the system with vacancies shows considerable dependence on the size of the simulation cell. Using a 40 atoms cell, the ground state turns out to be the triplet state, while using a 135 atoms simulation cell the ground state is singlet. This shows the strong spin-spin correlation prevalent in this oxide material which favors parallel spin orientation at higher defect concentration. We estimate the critical length-scale l_{c} to satisfy 7.89 Å$< l_{\mathrm{c}} <$ 11.84 Å. Correspondingly, there is a critical vacancy concentration (x_{v}) above which these spin correlations become important. Our best estimate for the lower and upper bound for the critical vacancy concentration is 6.03×10^{26} $\mathrm{m}^{-3} < x_{\mathrm{v}} <$ 2.01×10^{27} m^{-3}. These values are very close to the concentration of anionic defect reported along dislocation cores in $\mathrm{SrTiO_3}$ and at $\mathrm{LaAlO_3/SrTiO_3}$ interface.[8] For vacancy concentrations higher than x_{c} this hybridization will lead to enhanced local magnetic properties at these defect sites.[59]

There have been suggestions of existence of Ti^{3+} ions close to the vacancy.[60] However, our results point to a more covalent character in the bonding. This is in line with recent experimental results of Salluzzo at al.[61] The Ti-V_o-Ti hybridization in $\mathrm{SrTiO_3}$ is preferentially along the $\langle 100\rangle$ direction between the nearest neighbor Ti atoms. This breaks the symmetry of the lattice along the different $\langle 100\rangle$ directions. This can lead to large anisotropy in conductivity in $\mathrm{SrTiO_3}$ if oxygen vacancies are properly aligned. This hybridization scheme between the electrons and the nearest neighbor Ti ions in $\mathrm{SrTiO_3}$ is quite different from the electronic structure exhibited by oxides like ZrO_2 even though both Ti and Zr lie on the same column on the periodic table.[62] In $SrTiO_3$ the distance between the Ti and vacancy is $\sim$1.97 Å much smaller than the distance of 2.22 Å (lattice parameter 5.1276 Å) between the Zr and vacancy in ZrO_2.[4] This increase in bond length is similar to the increase in atomic size ($\sim 12\%$). This suggests that the nature of the Ti-O bond has more covalent character and is quite different from the nature of Zr-O bond in ZrO_2 or $SrZrO_3$.

Using molecular O_2 as the reference state, defect formation energies are obtained as a function of temperature and pressure. For a stable system, formation energy of a defect has to be positive. This puts a constrain on the accessible Fermi energy values. For example, at 800 K and 10^{-8} atm the allowed values of Fermi energy are 1.5-3.25 eV. However, a more stringent constrain is to maintain charge neutrality condition in the system even after formation of neutral or charged defects. From the ab-initio calculations of defect formation energies the rate constants for possible defect reaction equilibria are determined as a function of the temperature and oxygen partial pressure from the laws of mass action. The equilibrium defect concentrations are then determined by solving these reaction equilibria. We find that at low oxygen partial pressures doubly charged oxygen vacancies are dominant where as at higher oxygen pressures the interstitials are dominant. It is important to note that these defect concentrations are evaluated without accounting for defect interactions. Thus, in the high concentration limit, the actual concentrations can be different from those reported.

Fig. $12(b)$ shows the defect stability diagram at 1200 K as a function of oxygen partial pressure. At very low pressure the governing defect equilibria is

$$2\left[\mathrm{V_o^{2+}}\right] = \left[\mathrm{e^{1-}}\right]. \tag{23}$$

The dominant defect is the doubly charged oxygen vacancy and the singly charged oxygen vacancy has the second highest concentration. The Fermi energy of the system in this regime decreases with the increase in external pressure (or increase in electron concentration). Taking the concentration of anionic sites as $3/a_0^3$ = 4.89×10^{28} atoms/m^3, we obtain a defect concentration of 3.83×10^{21} defects/m^3 at 1200 K and 1 atm pressure and the electronic concentration is 7.66×10^{21} m^{-3}. Thus conductivity in this regime is governed by the electrons (n-type electronic conductivity). Further, the pressure dependence of the electronic concentration is $[\mathrm{e}^-] \propto P^{-1/6}$.

Acknowledgments

We acknowledge support by the Department of Energy under Grant No. de-sc0002623 and the Texas Advanced Computing Center (through TeraGrid) at The University of Texas at Austin for providing computing resources.

---

* Electronic address: `asamanta@math.princeton.edu`

[1] Y. Cui, X. F. Duan, J. T. Hu, and C. M. Lieber, Journal Of Physical Chemistry B **104**, 5213 (2000).

[2] S. B. Zhang, S. H. Wei, and A. Zunger, Physical Review B **63**, 075205 (2001).

[3] P. Aldebert and J. P. Traverse, Journal Of The American Ceramic Society **68**, 34 (1985).

[4] A. Samanta, T. Lenosky, and J. Li, arXiv:1009.5567 (2010).

[5] G. Brouwer, Philips Research Reports **9**, 366 (1954).

[6] M. W. Barsoum, Fundamentals of ceramics, Institute of Physics Publishing (1997).

[7] W. Gao and N. M. Sammes, An introduction to electronic and ionic materials, World Scientific Publishing (2000).

[8] K. Szot, W. Speier, R. Carius, U. Zastrow, and W. Beyer, Physical Review Letters **88**, 075508 (2002).

[9] M. Breitschaft, V. Tinkl, N. Pavlenko, S. Paetel, C. Richter, J. R. Kirtley, Y. C. Liao, G. Hammerl, V. Eyert, T. Kopp, et al., Physical Review B **81**, 153414 (2010).

[10] A. Dubroka, M. Rossle, K. W. Kim, V. K. Malik, L. Schultz, S. Thiel, C. W. Schneider, J. Mannhart, G. Herranz, O. Copie, et al., Physical Review Letters **104**, 156807 (2010).

[11] M. Ben Shalom, M. Sachs, D. Rakhmilevitch, A. Palevski, and Y. Dagan, Physical Review Letters **104**, 126802 (2010).

[12] A. D. Caviglia, M. Gabay, S. Gariglio, N. Reyren, C. Cancellieri, and J. M. Triscone, Physical Review Letters **104**, 126803 (2010).

[13] O. Copie, V. Garcia, C. Bodefeld, C. Carretero, M. Bibes, G. Herranz, E. Jacquet, J. L. Maurice, B. Vinter, S. Fusil, et al., Physical Review Letters **102**, 216804 (2009).

[14] A. B. Lidiard, Journal Of Nuclear Materials **19**, 106 (1966).

[15] H. Matzke, Journal Of The Chemical Society-Faraday Transactions Ii **83**, 1121 (1987).

[16] F. W. Poulsen, Journal Of Solid State Chemistry **143**, 115 (1999).

[17] Y. Tsur and C. A. Randall, Journal Of The American Ceramic Society **84**, 2147 (2001).

[18] R. Amin, C. T. Lin, J. B. Peng, K. Weichert, T. Acarturk, U. Starke, and J. Maier, Advanced Functional Materials **19**, 1697 (2009).

[19] K. L. Duncan and E. D. Wachstnan, Ionics **13**, 127 (2007).

[20] S. B. Zhang and J. E. Northrup, Physical Review Letters **67**, 2339 (1991).

[21] J. P. Crocombette, F. Jollet, L. T. Nga, and T. Petit, Physical Review B **64**, 104107 (2001).

[22] S. B. Zhang, Journal Of Physics-Condensed Matter **14**, R881 (2002).
[23] J. P. Crocombette, D. Torumba, and A. Chartier, Physical Review B **83**, 184107 (2011).
[24] K. Benthem, C. Elsasser, and R. H. French, Journal of Applied Physics **90**, 6156 (2001).
[25] L. Gracia, J. Andres, V. M. Longo, J. A. Varela, and E. Longo, Chemical Physics Letters **493**, 141 (2010).
[26] V. M. Longo, A. T. de Figueiredo, S. de Lazaro, M. F. Gurgel, M. G. S. Costa, C. O. Paiva-Santos, J. A. Varela, E. Longo, V. R. Mastelaro, F. S. De Vicente, et al., Journal Of Applied Physics **104**, 023515 (2008).
[27] D. D. Cuong, B. Lee, K. M. Choi, H. S. Ahn, S. Han, and J. Lee, Physical Review Letters **98**, 115503 (2007).
[28] G. Kresse and J. Furthmuller, Physical Review B **54**, 11169 (1996).
[29] G. Kresse and J. Furthmuller, Computational Materials Science **6**, 15 (1996).
[30] G. Kresse and D. Joubert, Physical Review B **59**, 1758 (1999).
[31] L. D. Madsen, C. N. L. Johnson, S. N. Jacobsen, U. Helmersson, S. Rudner, I. Ivanov, L. D. Wernlund, L. Ryen, and E. Olsson, Microelectronic Engineering **29**, 123 (1995).
[32] E. J. Tarsa, E. A. Hachfeld, F. T. Quinlan, J. S. Speck, and M. Eddy, Applied Physics Letters **68**, 490 (1996).
[33] J. Kim, Y. Kim, Y. S. Kim, J. Lee, L. Kim, and D. Jung, Applied Physics Letters **80**, 3581 (2002).
[34] T. Shimuta, O. Nakagawara, T. Makino, S. Arai, H. Tabata, and T. Kawai, Journal Of Applied Physics **91**, 2290 (2002).
[35] G. Henkelman, B. P. Uberuaga, and H. Jonsson, Journal Of Chemical Physics **113**, 9901 (2000).
[36] H. Yamada and G. R. Miller, Journal Of Solid State Chemistry **6**, 169 (1973).
[37] M. Leonhardt, J. Jamnik, and J. Maier, Electrochemical And Solid State Letters **2**, 333 (1999).
[38] T. Sano, D. M. Saylor, and G. S. Rohrer, Journal Of The American Ceramic Society **86**, 1933 (2003).
[39] K. Szot, W. Speier, G. Bihlmayer, and R. Waser, Nature Materials **5**, 312 (2006).
[40] V. I. Vedeneyev, L. V. Gurvich, M. V. A. Kondratyev, V. N., and Y. L. Frankevich, *Bond Energies, Ionization Potentials and Electron Affinities* (St. Martin's Press, New York, 1962).
[41] D. A. McQuarrie, Statistical Mechanics, Harper Collins Publishers (1976).
[42] D. S. Villars, Proceedings of the National Academy of Sciences **15**, 705 (1929).
[43] P. Pasierb, S. Komornicki, and M. Rekas, Journal Of Physics And Chemistry Of Solids **60**, 1835 (1999).
[44] F. Cordero, Physical Review B **76**, 172106 (2007).
[45] M. Lontsi-Fomena, A. Villesuzanne, J. P. Doumerc, C. Frayret, and M. Pouchard, Computational Materials Science **44**, 53 (2008).
[46] F. Cordero, Materials Science And Engineering A-Structural Materials Properties Microstructure And Processing **521-22**, 77 (2009).
[47] R. Astala and P. D. Bristowe, Modelling And Simulation In Materials Science And Engineering **9**, 415 (2001).
[48] D. Ricci, G. Bano, G. Pacchioni, and F. Illas, Physical Review B **68**, 224105 (2003).
[49] E. Heifets, S. Piskunov, E. A. Kotomin, Y. F. Zhukovskii, and D. E. Ellis, Physical Review B **75**, 115417 (2007).
[50] T. Leisegang, H. Stocker, A. A. Levin, T. Weissbach, M. Zschornak, E. Gutmann, K. Rickers, S. Gemming, and D. C. Meyer, Physical Review Letters **102** 087601 (2009).
[51] S. X. Tian, Journal Of Physical Chemistry B **108**, 20388 (2004).
[52] V. I. Avdeev, S. F. Ruzankin, and G. M. Zhidomirov, Journal Of Structural Chemistry **38**, 519 (1997).
[53] E. Sanville, S. D. Kenny, R. Smith, and G. Henkelman, Journal Of Computational Chemistry **28**, 899 (2007).
[54] G. Henkelman, A. Arnaldsson, and H. Jonsson, Computational Materials Science **36**, 354 (2006).
[55] The net charge on other ions differ by less than 0.15e from their in a pure structure.
[56] T. Brudevoll, E. A. Kotomin, and N. E. Christensen, Physical Review B **53**, 7731 (1996).
[57] Z. C. Wang, S. Karato, and K. Fujino, Physics Of The Earth And Planetary Interiors **79**, 299 (1993).
[58] D. Singh, M. Lorenzo-Martin, G. Chen, F. Gutierrez-Mora, and J. L. Routbort, Journal Of The European Ceramic Society **27**, 3377 (2007).
[59] A. Brinkman, M. Huijben, M. Van Zalk, J. Huijben, U. Zeitler, J. C. Maan, W. G. Van der Wiel, G. Rijnders, D. H. A. Blank, and H. Hilgenkamp, Nature Materials **6**, 493 (2007).
[60] S. Okamoto, A. J. Millis, and N. A. Spaldin, Physical Review Letters **97**, 056802 (2006).
[61] M. Salluzzo, J. C. Cezar, N. B. Brookes, V. Bisogni, G. M. Luca, C. Richter, S. Thiel, J. Mannhart, M. Huijben, A. Brinkman, et al., Physical Review Letters **102**, 166804 (2009).
[62] G. Stapper, M. Bernasconi, N. Nicoloso, and M. Parrinello, Physical Review B **59**, 797 (1999).

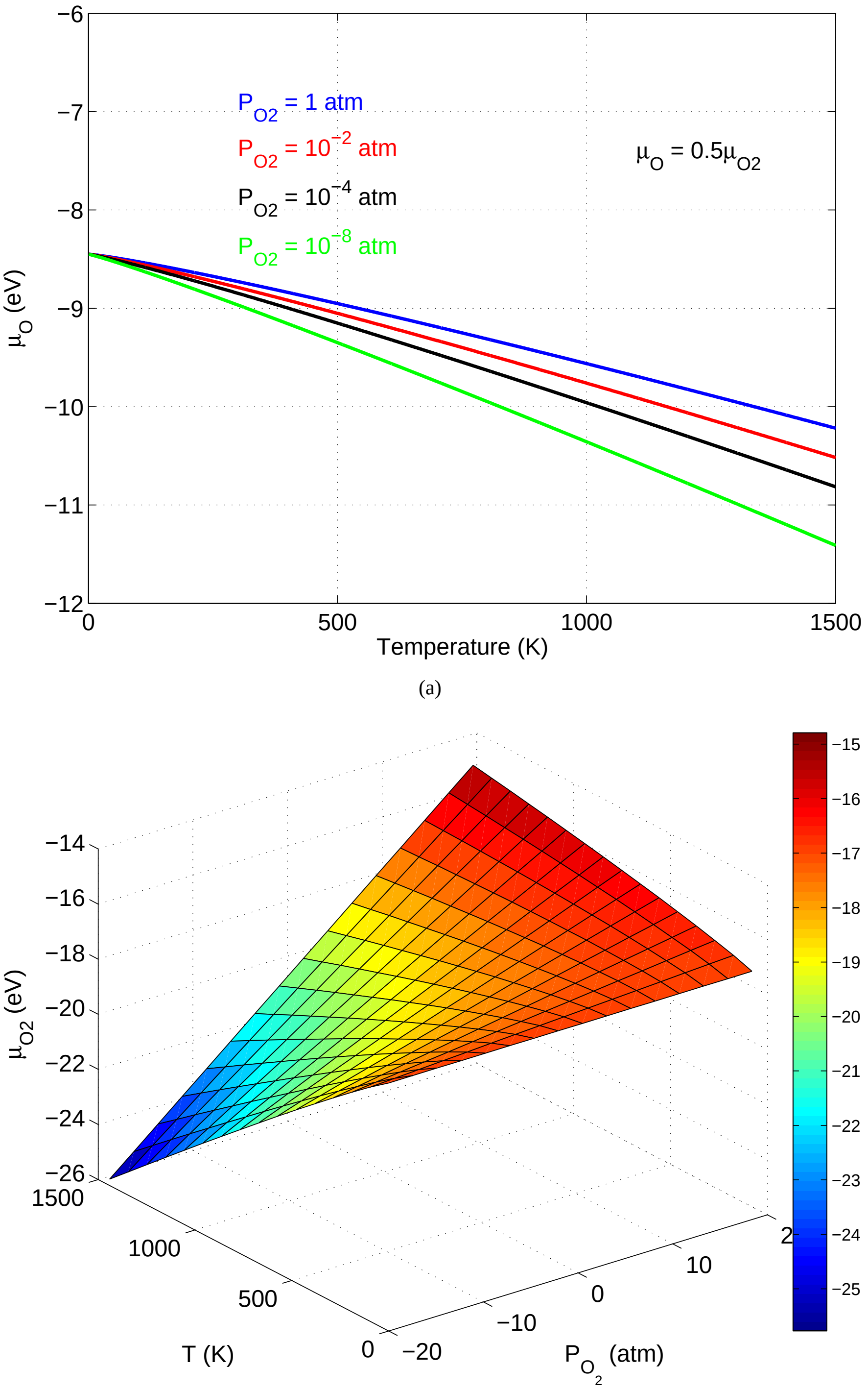

(a)

(b)

FIG. 1: The chemical potential of an oxygen atom (Fig. $1(a)$) and oxygen molecule (Fig. $1(b)$) as a function of temperature at different oxygen partial pressures calculated from the quantum formulation of an ideal gas. $(\mu_{\rm O} = 0.5\mu_{\rm O_2})$ At a given temperature the chemical potentials decreases with decrease in oxygen partial pressure.

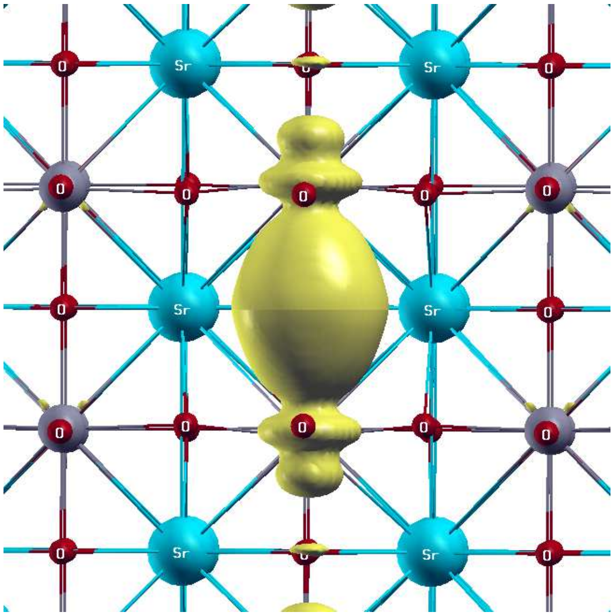

FIG. 2: Spin density profile for an oxygen vacancy in a singly charged simulation cell shows the hybridization between the two Ti ions and electrons at the vacant oxygen site at isosurface value of 0.01 e/Å^3.

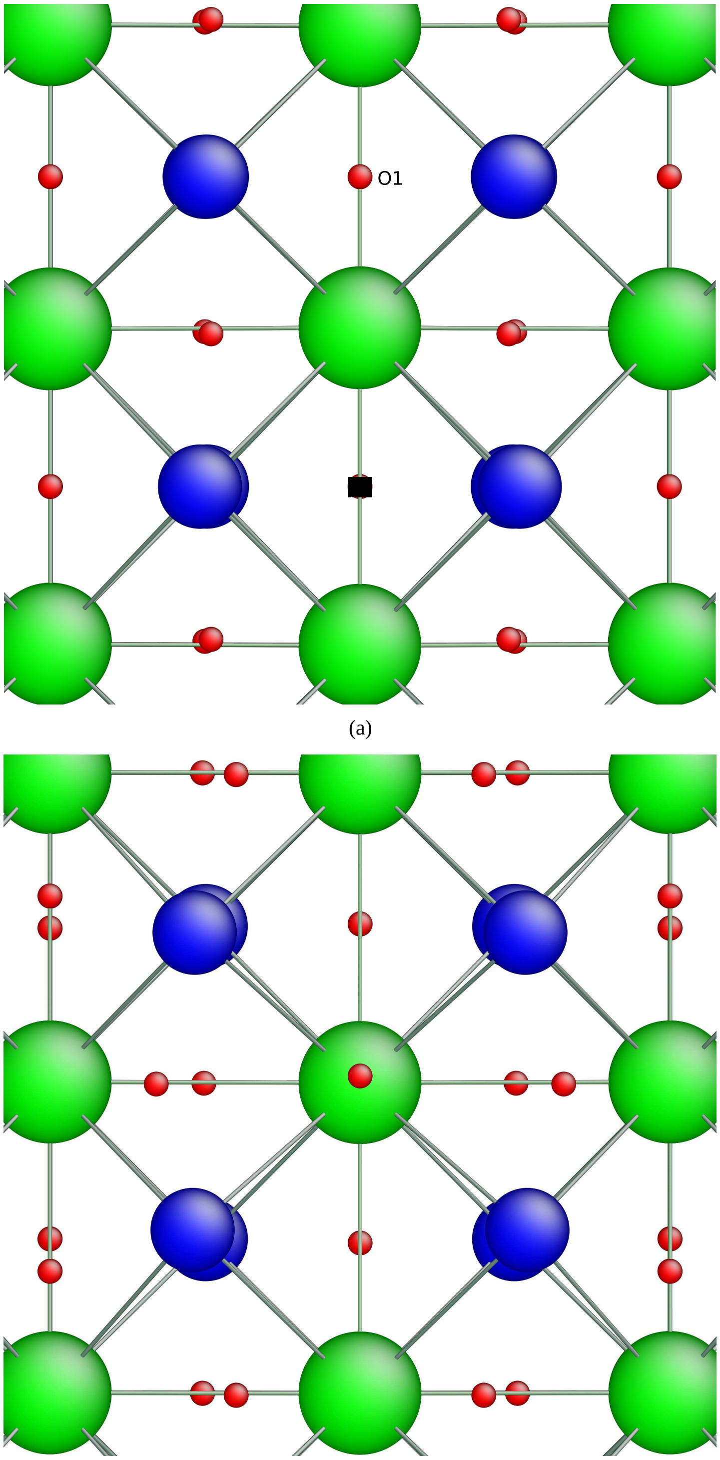

(a)

(b)

FIG. 3: Snapshots of intermediate configurations for diffusion of oxygen vacancy along $\langle 100 \rangle$ path in a neutral cell in a neutral cell viewed along $\langle 100 \rangle$ direction. $3(a)$ initial structure, oxygen vacancy is marked with a black square. The nearest neighbor oxygen (marked O1) is involved in the diffusion process. $3(b)$ is the saddle configuration. (O is in red, Ti is in blue and Sr is in green.)

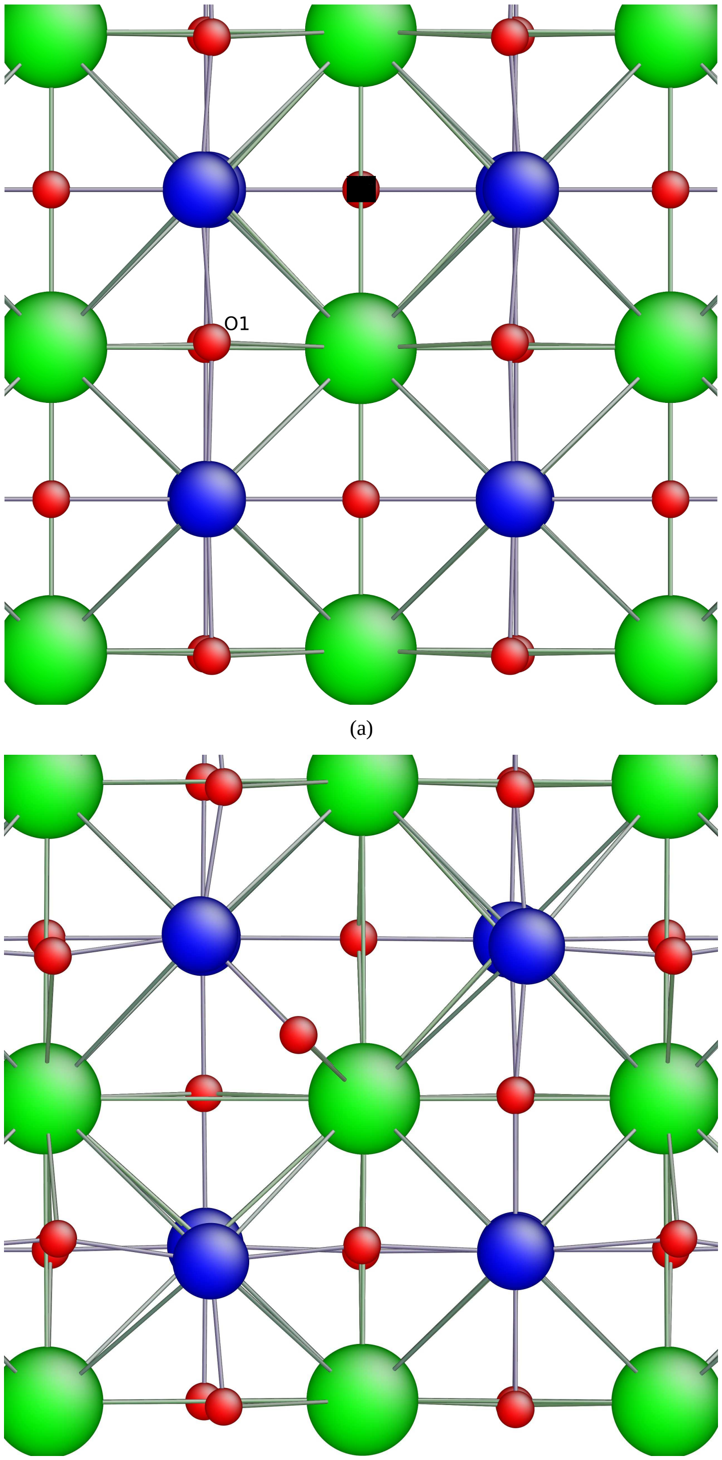

(a)

(b)

FIG. 4: Snapshots of intermediate configurations for diffusion of oxygen vacancy along $\langle 110 \rangle$ path in a neutral cell viewed along $\langle 100 \rangle$ direction. $4(a)$ initial structure, oxygen vacancy is marked with a black square. The nearest neighbor oxygen (marked O1) is involved in the diffusion process. $4(b)$ is the saddle configuration. (O is in red, Ti is in blue and Sr is in green.)

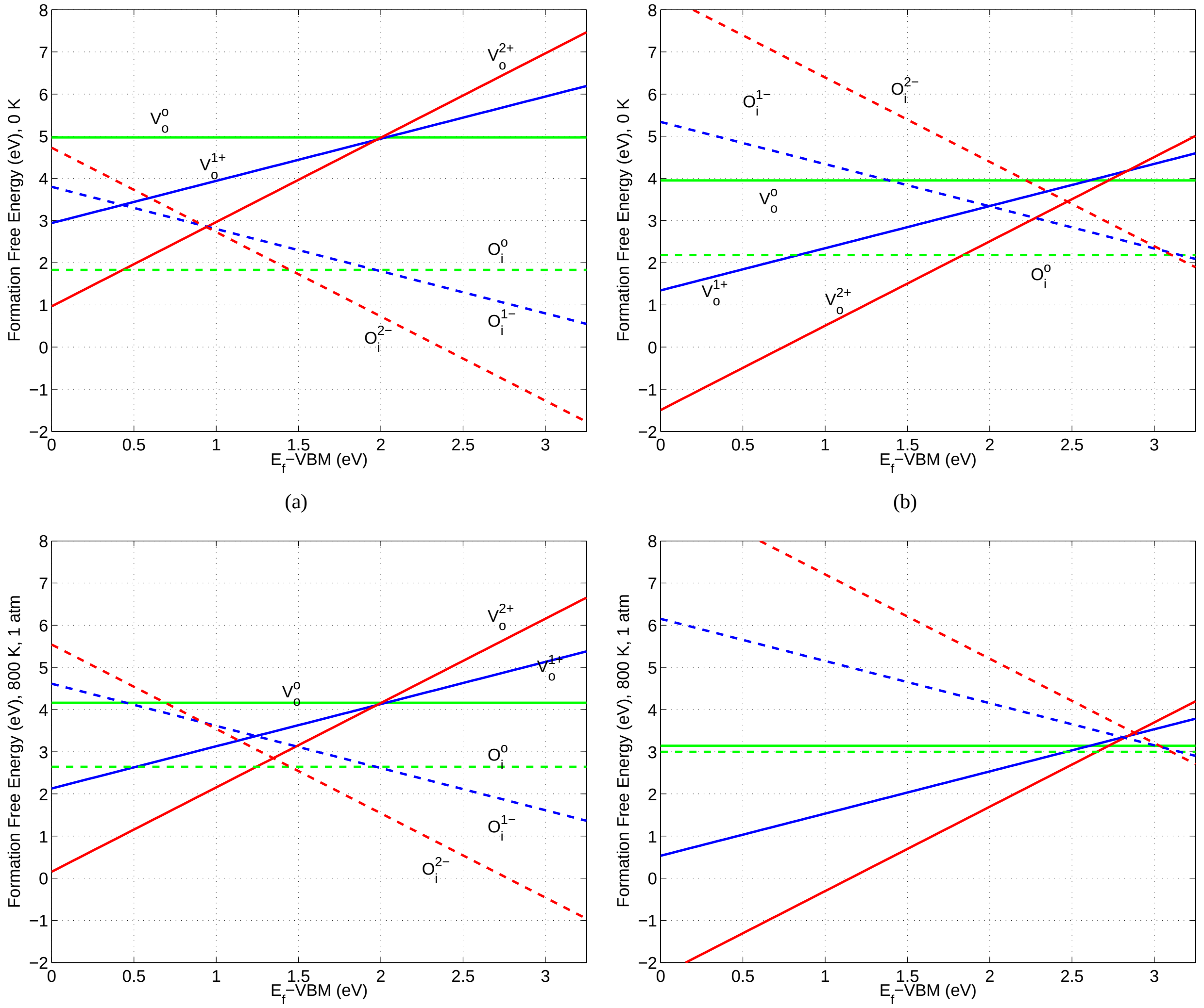

(a)

(b)

(c)

(d)

FIG. 5: Point defect formation energies, obtained from results of PBE and HSE calculations, at 0 K and 800 K and different oxygen partial pressures: $5(a)$ PBE functional and $5(b)$ HSE hybrid functional at 0 K and zero pressure, $5(c)$ PBE functional and $5(d)$ HSE hybrid functional at 800 K and 1 atm.

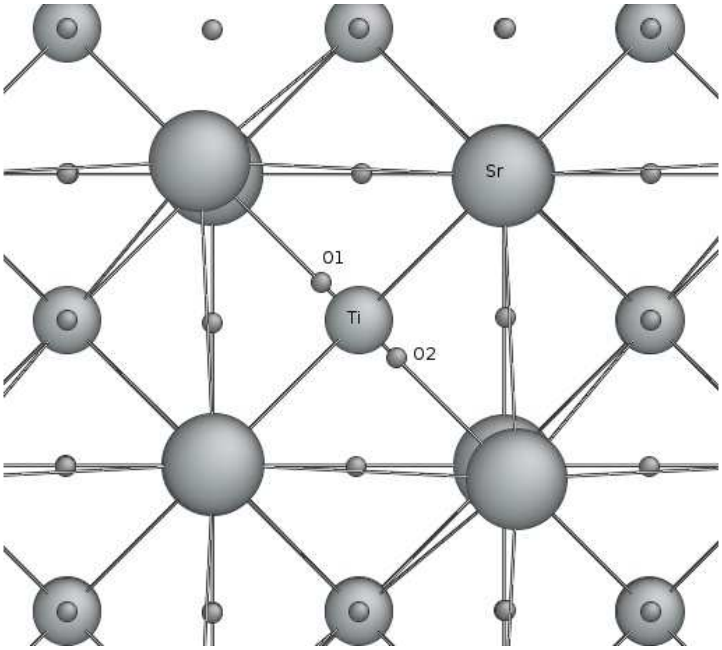

(a)

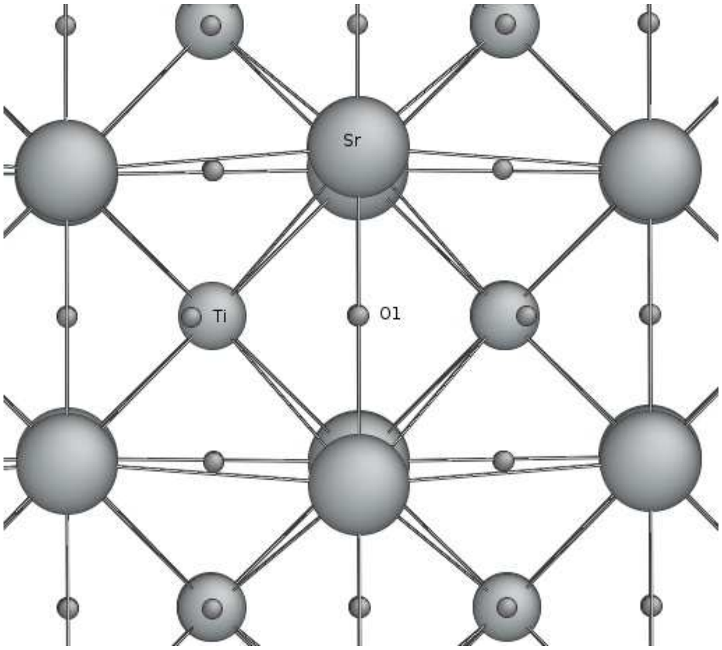

(b)

FIG. 6: Snapshots of oxygen interstitial configurations in $SrTiO_3$ viewed along $\langle 100 \rangle$ direction. $6(a)$ $\langle 110 \rangle$ dumbbell configuration of neutral oxygen interstitial. $6(b)$ $\langle 100 \rangle$ crowd-ion configurations of neutral oxygen interstitial (denoted by O1 in the figure).

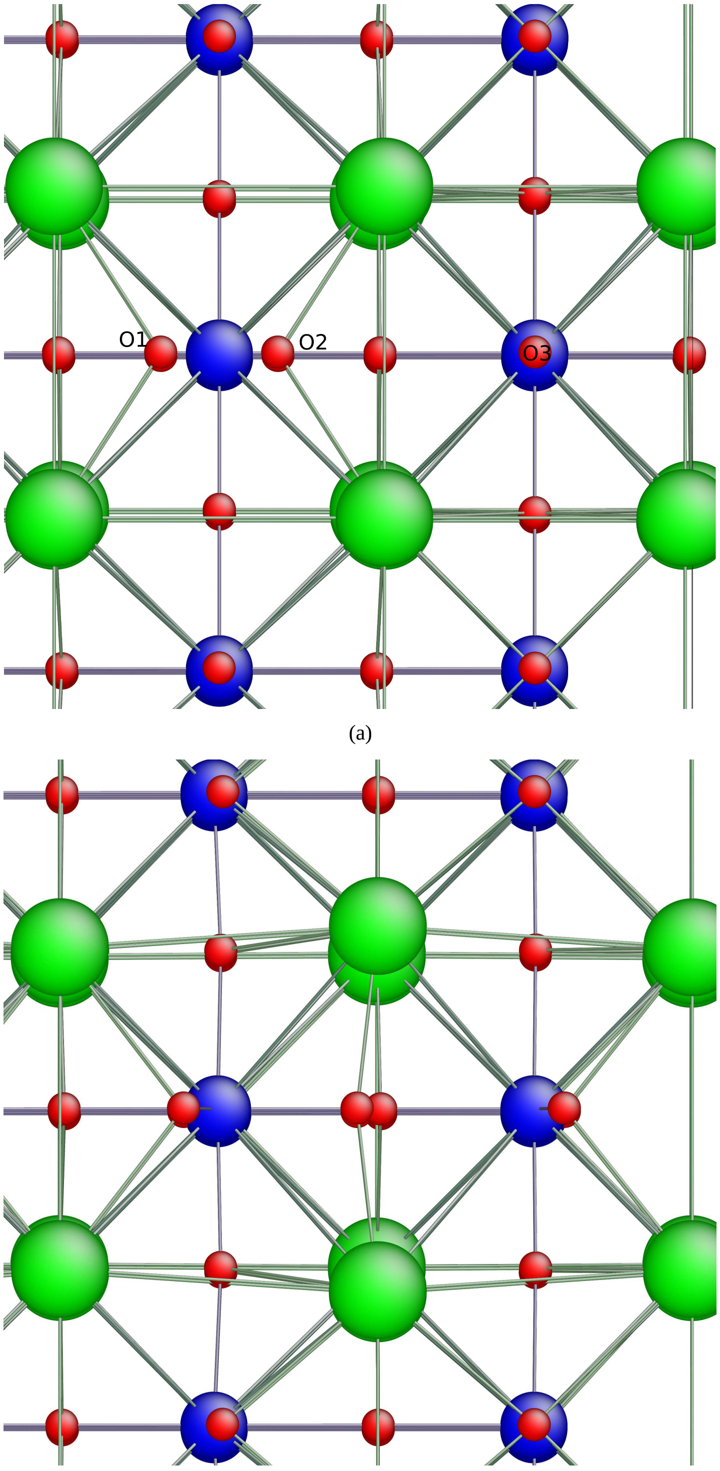

(a)

(b)

FIG. 7: Snapshots of (100) plane of intermediate configurations for diffusion of an oxygen interstitial in a neutral cell along $\langle 100 \rangle$ direction. $7(a)$ initial structure with the $\langle 100 \rangle$ dumbbell and $7(b)$ corresponds to the saddle configuration. (O is in red, Ti is in blue and Sr is in green.)

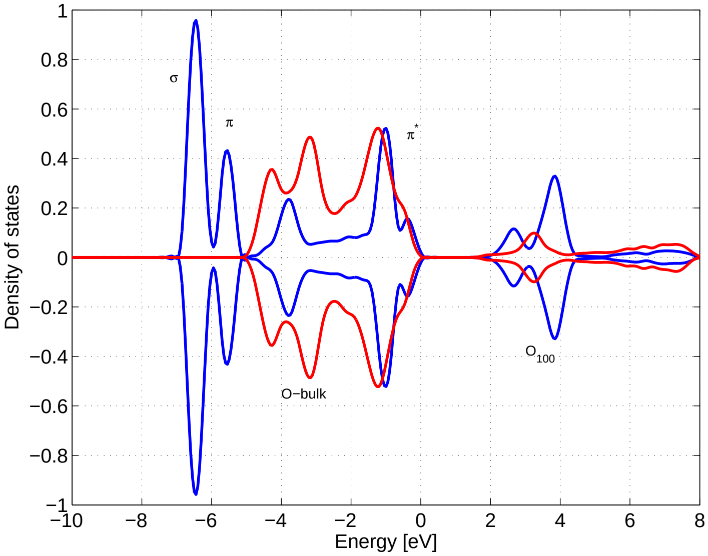

(a)

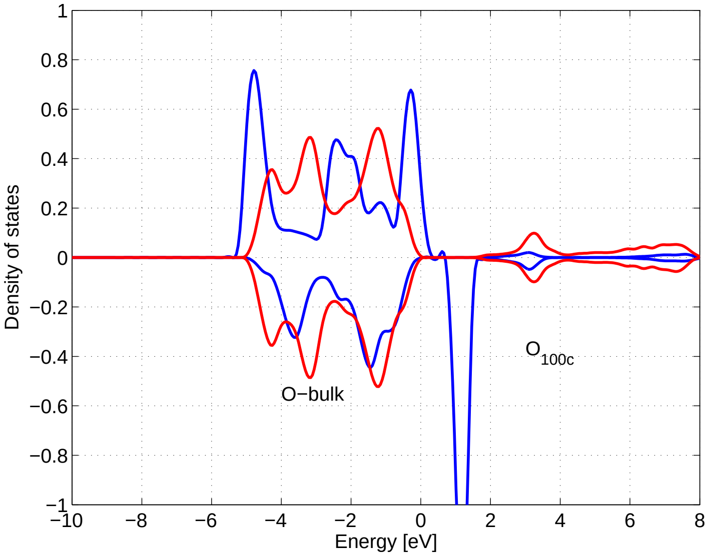

(b)

FIG. 8: $8(a)$ Comparison of the site projected density of states for an oxygen ion in $\langle 100 \rangle$ dumbbell in a neutral cell and oxygen ion in a defect free configuration. The energy levels are marked with corresponding molecular energy levels of oxygen molecule. $8(b)$ Comparison of the site projected density of states for an oxygen ion in $\langle 100 \rangle$ crowd-ion configuration in a neutral cell and oxygen ion in a defect free configuration.

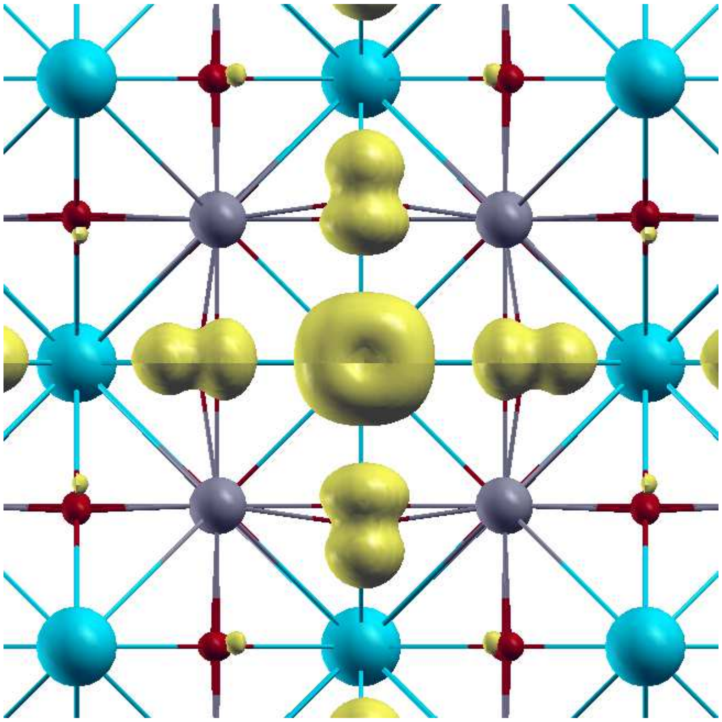

FIG. 9: Charge density isosurface at 0.02 e/Å^3 for oxygen interstitial in $\langle 100 \rangle$ crowd-ion configuration in a neutral cell.

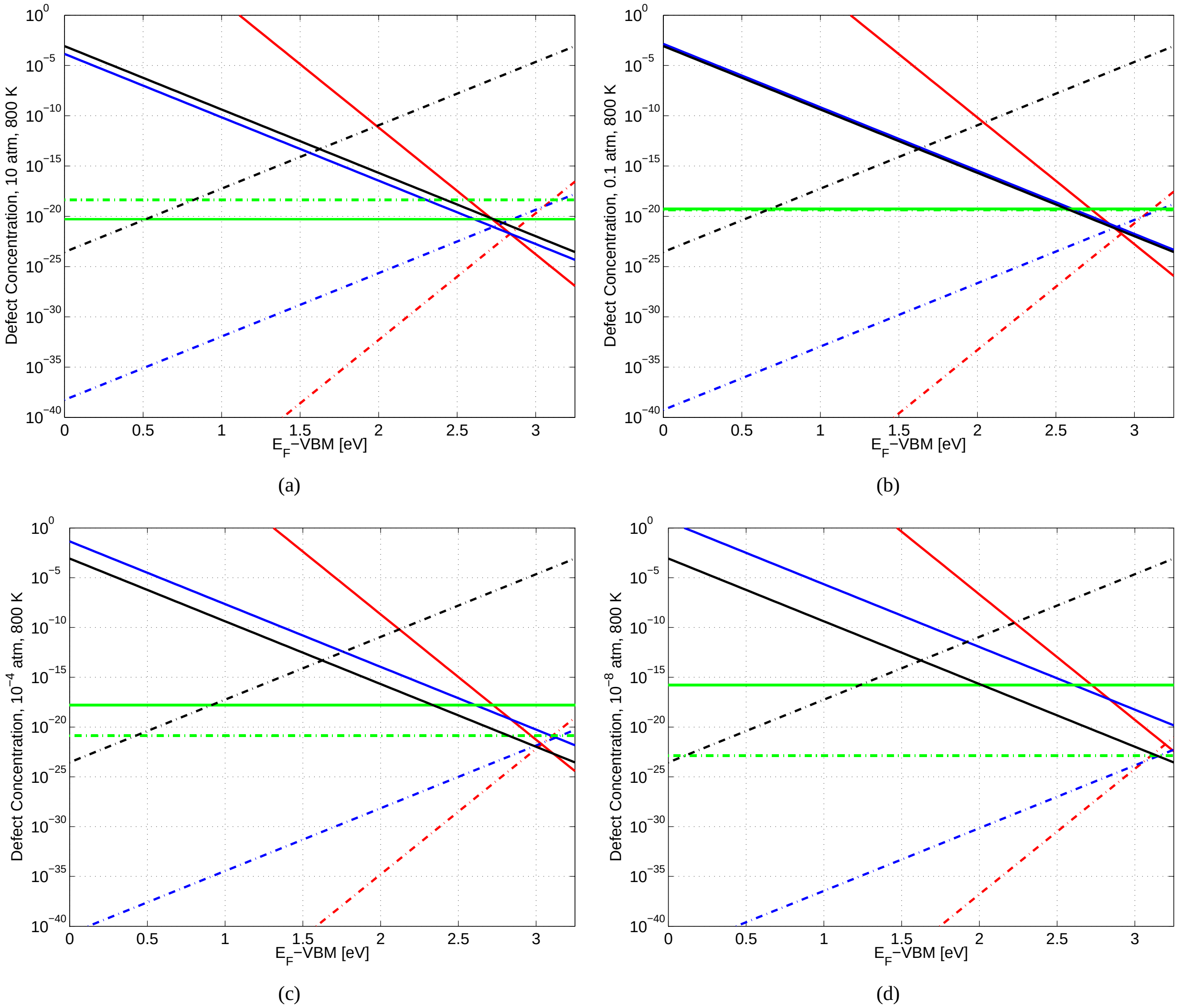

(a)

(b)

(c)

(d)

FIG. 10: Defect concentration profiles obtained by using HSE hybrid functional at 800 K and different oxygen partial pressures: $10(a)$ at 10^1 atm, $10(b)$ at 10^{-1} atm, $10(c)$ at 10^{-4} atm and $10(d)$ at 10^{-8} atm. In the figures, the solid black line is $[\mathrm{h}^+]$, black dash line is $[\mathrm{e}^-]$, solid red line is $[\mathrm{V_o^{2+}}]$, red dash line is $[\mathrm{O_i^{2-}}]$, blue line is $[\mathrm{V_o^{1+}}]$, blue dash line is $[\mathrm{O_i^{1-}}]$, green line is $[\mathrm{V_o}]$ and green dash line is $[\mathrm{O_i}]$. The reference state is an oxygen gas molecule at 800 K and the defect concentrations are expressed as fraction of total anionic sites in $\mathrm{SrTiO_3}$.

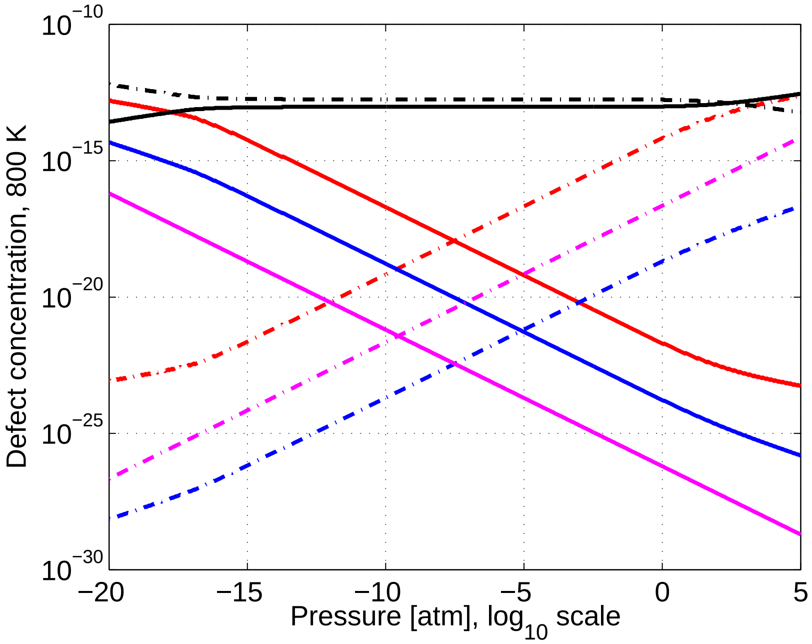

(a)

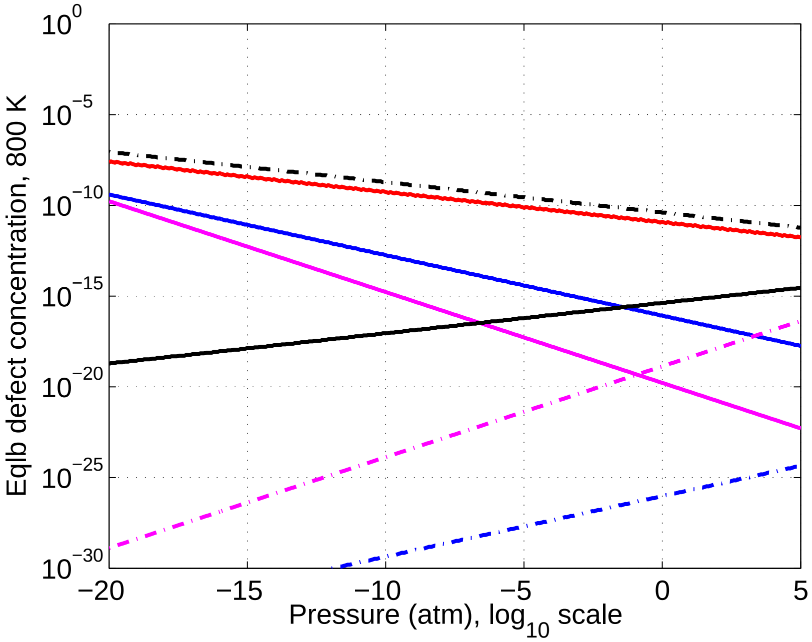

(b)

FIG. 11: Equilibrium defect concentration profiles (expressed as fraction of total anionic sites) at 800 K obtained from $(11(a))$ PBE functional and $11(b)$ HSE hybrid functional calculations, as a function of oxygen partial pressure obtained by solving the different reaction equilibria. The defect levels in Fig. $11(a)$ are not scaled and the defect concentrations are assumed to be in their dilute limit. The reference state is an oxygen gas molecule. In the figures, the solid black line is $[\mathrm{h}^{+}]$, black dash line is $[\mathrm{e}^{-}]$, solid red line is $[\mathrm{V}_{\mathrm{o}}^{2+}]$, red dash line is $[\mathrm{O}_{\mathrm{i}}^{2-}]$, blue line is $[\mathrm{V}_{\mathrm{o}}^{1+}]$, blue dash line is $[\mathrm{O}_{\mathrm{i}}^{1-}]$, green line is $[\mathrm{V}_{\mathrm{o}}]$ and green dash line is $[\mathrm{O}_{\mathrm{i}}]$.

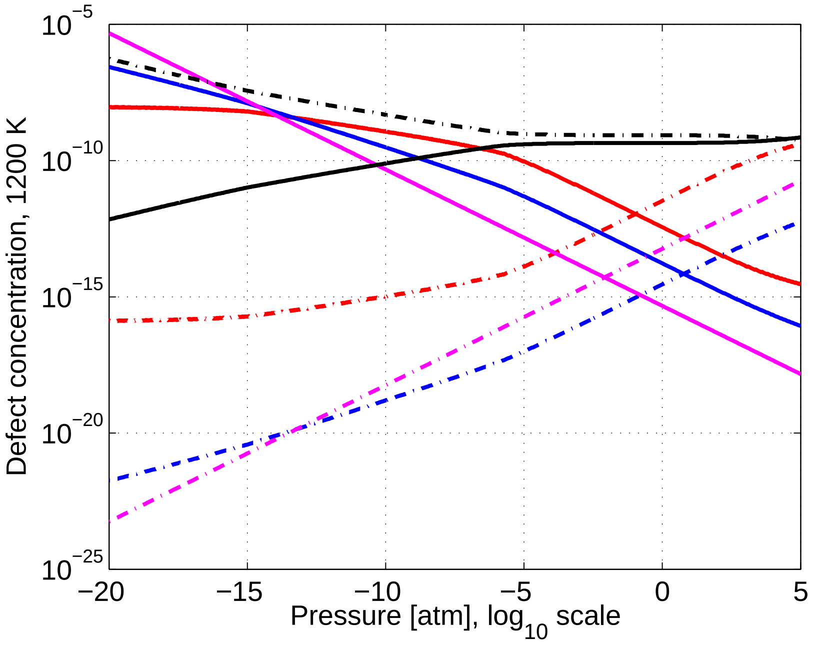

(a)

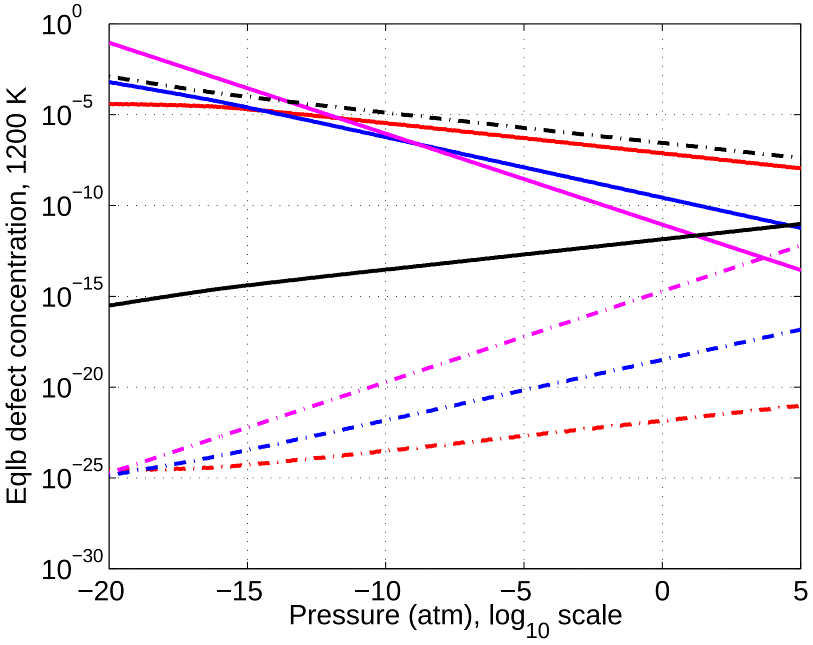

(b)

FIG. 12: Equilibrium defect concentration profiles (expressed as fraction of total anionic sites), obtained from $12(a)$ PBE functional and $12(b)$ HSE hybrid functional calculations, as a function of oxygen partial pressure at 1200 K. The defect levels in Fig. $12(a)$ are not scaled and the defect concentrations are assumed to be in their dilute limit. The reference state is an oxygen gas molecule. In the figures, the solid black line is $[\mathrm{h}^{+}]$, black dash line is $[\mathrm{e}^{-}]$, solid red line is $[\mathrm{V}_{\mathrm{o}}^{2+}]$, red dash line is $[\mathrm{O}_{\mathrm{i}}^{2-}]$, blue line is $[\mathrm{V}_{\mathrm{o}}^{1+}]$, blue dash line is $[\mathrm{O}_{\mathrm{i}}^{1-}]$, green line is $[\mathrm{V}_{\mathrm{o}}]$ and green dash line is $[\mathrm{O}_{\mathrm{i}}]$.

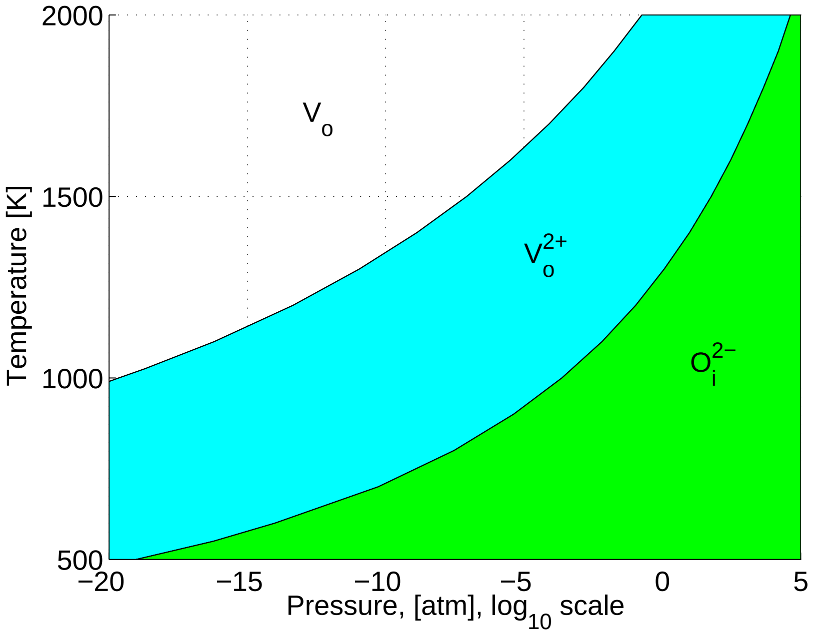

(a)

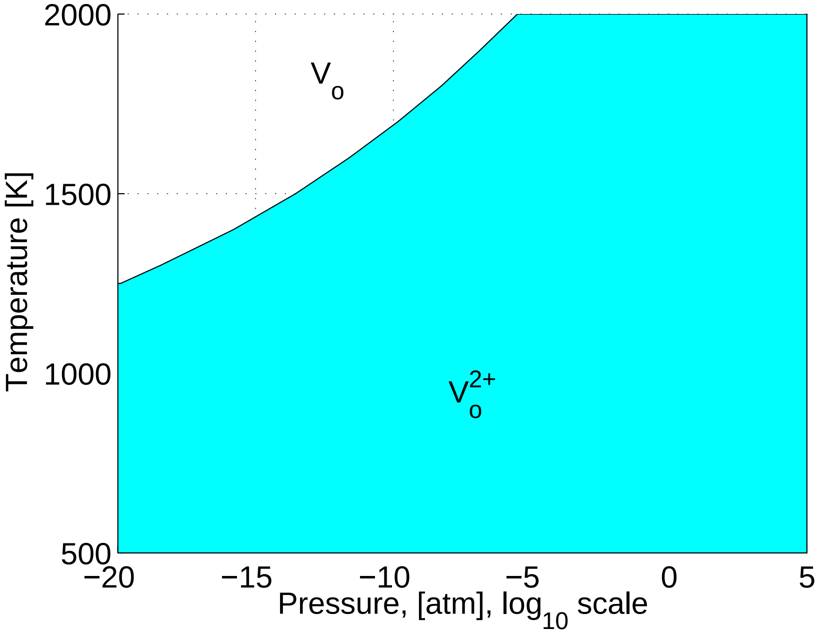

(b)

FIG. 13: Equilibrium defect stability phase diagram for anionic defects in undoped $SrTiO_3$ obtained by using PBE exchange correlation functional. In Fig. $13(a)$ the defect levels are not scaled while in $13(b)$ defect levels are scaled by the ratio of experimental band-gap to PBE functional band-gap.

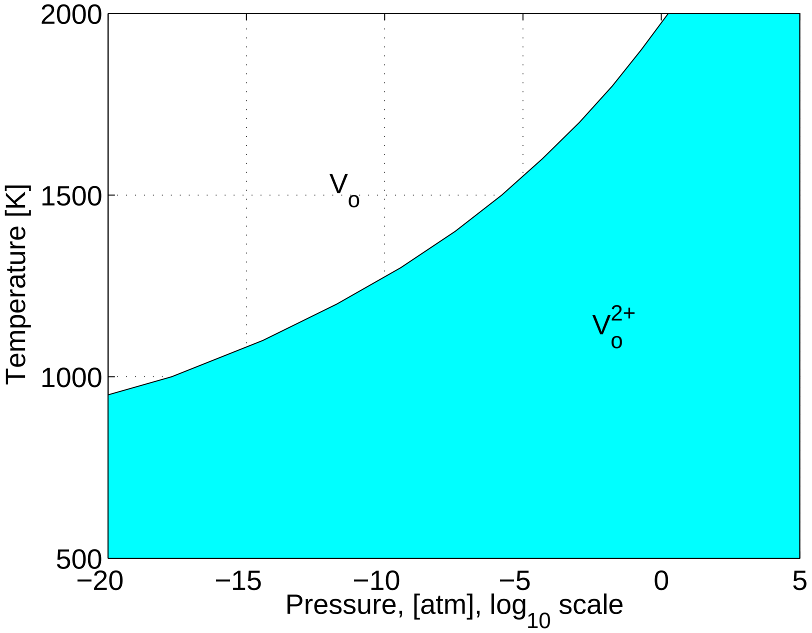

FIG. 14: Equilibrium defect stability phase diagram for anionic defects in undoped $SrTiO_3$ obtained by using HSE hybrid functional.